

# Behaviour of the Dam-Break Problem for the Serre Equations

Jordan Pitt,<sup>1</sup>  
Christopher Zoppou,<sup>1</sup>  
Stephen G. Roberts,<sup>1</sup>

## ABSTRACT

**Keywords:** dispersive waves, conservation laws, Serre equation, finite volume method, finite difference method

## INTRODUCTION

### SERRE EQUATIONS

The Serre equations can derived as an approximation to the full Euler equations by depth integration similar to (Su and Gardner 1969). They can also be seen as an asymptotic expansion of the Euler equations (Lannes and Bonneton 2009). The former is more consistent with the perspective from which numerical methods will be developed while the latter indicates the appropriate regions in which to use these equations as a model for fluid flow. The scenario under which the Serre approximation is made consists of a two dimensional  $\mathbf{x} = (x, z)$  fluid over a bottom topography as in Figure 1 acting under gravity. Consider a fluid particle at depth  $\xi(\mathbf{x}, t) = h(x, t) + z_b(x) - z$  below the water surface, see Figure 1. Where the water depth is  $h(x, t)$  and  $z_b(x)$  is the bed elevation. The fluid particle is subject to the pressure,  $p(\mathbf{x}, t)$  and gravitational acceleration,  $\mathbf{g} = (0, g)^T$  and has a velocity  $\mathbf{u} = (u(\mathbf{x}, t), w(\mathbf{x}, t))$ , where  $u(\mathbf{x}, t)$  is the velocity in the  $x$ -coordinate and  $w(\mathbf{x}, t)$  is the velocity in the  $z$ -coordinate and  $t$  is time. Assuming that  $z_b(x)$  is constant the Serre equations read (Li et al. 2014)

$$\frac{\partial h}{\partial t} + \frac{\partial(\bar{u}h)}{\partial x} = 0 \quad (1a)$$

$$\underbrace{\frac{\partial(\bar{u}h)}{\partial t} + \frac{\partial}{\partial x} \left( \bar{u}^2 h + \frac{gh^2}{2} \right)}_{\text{Shallow Water Wave Equations}} + \underbrace{\frac{\partial}{\partial x} \left( \frac{h^3}{3} \left[ \frac{\partial \bar{u}}{\partial x} \frac{\partial \bar{u}}{\partial x} - \bar{u} \frac{\partial^2 \bar{u}}{\partial x^2} - \frac{\partial^2 \bar{u}}{\partial x \partial t} \right] \right)}_{\text{Dispersion Terms}} = 0. \quad (1b)$$

Serre Equations

Where  $\bar{u}$  is the average of  $u$  over the depth of water.

<sup>1</sup>Mathematical Sciences Institute, Australian National University, Canberra, ACT 0200, Australia, E-mail: Jordan.Pitt@anu.edu.au. The work undertaken by the first author was supported financially by an Australian National University Scholarship.

22 **Conservation of mass and momentum**

23 The Serre equations are based on conservation of mass and momentum, thus our nu-  
24 mercial methods should reflect this property. The total of a quantity  $q$  in a system is  
25 measured by

$$C_q(t) = \int_{-\infty}^{\infty} q \, dx \quad (2)$$

26 so that we have for all  $t$  both  $C_h(0) = C_h(t)$  and  $C_{\bar{u}h}(0) = C_{\bar{u}h}(t)$  representing conservation  
27 of mass and momentum respectively.

28 **Hamiltonian**

29 The Serre equations admit a Hamiltonian (Li 2002; Le Métayer et al. 2010; Green and  
30 Naghdi 1976)

$$\mathcal{H}(t) = \frac{1}{2} \int_{-\infty}^{\infty} hu^2 + gh^2 + \frac{h^3}{3} \left( \frac{\partial u}{\partial x} \right)^2 \, dx \quad (3)$$

31 where the bar over  $u$  has been dropped to simplify notation. The Hamiltonian is such that  
32  $\mathcal{H}(t) = \mathcal{H}(0)$  for all times  $t$ .

33 We can calculate this numerically by partitioning the total integral into cell-wise in-  
34 tegrals. The cell-wise integral can then be calculated by quartic interpolation utilising  
35 neighbouring cells and then applying Gaussian quadrature with 3 points over the cell to  
36 get a sufficiently high order method to calculate the Hamiltonian, in particular this method  
37 is at least third order accurate for the  $\partial u / \partial x$  term.

38 **DIRECT NUMERICAL METHODS**

39 The presence of the mixed spatial temporal derivatives in the momentum equation (1b)  
40 makes the Serre equations difficult to solve with standard numerical methods. A naive  
41 way to avoid this is to approximate (1b) by finite differences and the results of this are  
42 presented here. To facilitate this a uniform grid in space will be used with  $\Delta x = x_{i+1} - x_i$   
43 for all  $i$ . Quantities evaluated at these grid points will be denoted by subscripts for example  
44  $h_i = h(x_i)$ . The grid in time is also uniform and will be denoted by superscripts for example  
45  $h^n = h(t^n)$ , note that  $h^n$  is a function in space.

46 **Finite Difference Appximation to Conservation of Momentum Equation**

47 In [][Zoppou thesis/my work] it was demonstrated that an efficient numerical scheme  
48 for the Serre equations must be at least second-order accurate thus the derivatives in (1b)

49 will be approximated by second-order finite differences. Firstly (1b) must be expanded,  
50 making use of (1a) one obtains

$$51 \quad h \frac{\partial u}{\partial t} + X - h^2 \frac{\partial^2 u}{\partial x \partial t} - \frac{h^3}{3} \frac{\partial^3 u}{\partial x^2 \partial t} = 0 \quad (4a)$$

52 where  $X$  contains only spatial derivatives and is

$$53 \quad X = uh \frac{\partial u}{\partial x} + gh \frac{\partial h}{\partial x} + h^2 \frac{\partial u}{\partial x} \frac{\partial u}{\partial x} + \frac{h^3}{3} \frac{\partial u}{\partial x} \frac{\partial^2 u}{\partial x^2} - h^2 u \frac{\partial^2 u}{\partial x^2} - \frac{h^3}{3} u \frac{\partial^3 u}{\partial x^3}. \quad (4b)$$

54 Taking the second-order centred finite difference approximation to the spatial and temporal  
55 derivatives for (4a) after some rearranging gives

$$56 \quad h_i^n u_i^{n+1} - (h_i^n)^2 \left( \frac{u_{i+1}^{n+1} - u_{i-1}^{n+1}}{2\Delta x} \right) - \frac{(h_i^n)^3}{3} \left( \frac{u_{i+1}^{n+1} - 2u_i^{n+1} + u_{i-1}^{n+1}}{\Delta x^2} \right) = -Y_i^n \quad (5)$$

57 where

$$58 \quad Y_i^n = 2\Delta t X_i^n - h_i^n u_i^{n-1} + (h_i^n)^2 \left( \frac{u_{i+1}^{n-1} - u_{i-1}^{n-1}}{2\Delta x} \right) + \frac{(h_i^n)^3}{3} \left( \frac{u_{i+1}^{n-1} - 2u_i^{n-1} + u_{i-1}^{n-1}}{\Delta x^2} \right).$$

59 Equation (5) can be rearranged into a tri-diagonal matrix that updates  $u$  given its current  
60 and previous values. So that

$$61 \quad \begin{bmatrix} u_0^{n+1} \\ \vdots \\ u_m^{n+1} \end{bmatrix} = A^{-1} \begin{bmatrix} -Y_0^n \\ \vdots \\ -Y_m^n \end{bmatrix} =: \mathcal{G}_u(u^n, h^n, u^{n-1}, h^{n-1}, \Delta x, \Delta t). \quad (6)$$

62 In particular this is an explicit [?] numerical method for (1b), that requires the current and  
63 previous values of  $h$  and  $u$ .

### 64 The Lax-Wendroff Method for Conservation of Mass Equation

65 Because the conservation of mass equation (1a) has no mixed derivative term standard  
66 numerical techniques for conservation laws can be used. In particular the Lax-Wendroff  
67 method can be used as done by El et al. (2006), here we present the method in replicable  
68 detail.

69 Note that (1a) is in conservative law form for  $h$  where the flux is  $uh$ . Thus using the  
70 previously defined spatio-temporal discretisation the two step Lax-Wendroff update[] for  
71  $h$  is

$$72 \quad h_{i+1/2}^{n+1/2} = \frac{1}{2} (h_{i+1}^n + h_i^n) - \frac{\Delta t}{2\Delta x} (u_{i+1}^n h_{i+1}^n - h_i^n u_i^n), \quad (7)$$

$$80 \quad h_{i-1/2}^{n+1/2} = \frac{1}{2} (h_i^n + h_{i-1}^n) - \frac{\Delta t}{2\Delta x} (u_i^n h_i^n - h_{i-1}^n u_{i-1}^n), \quad (8)$$

$$83 \quad h_i^{n+1} = h_i^n - \frac{\Delta t}{\Delta x} (u_{i+1/2}^{n+1/2} h_{i+1/2}^{n+1/2} - u_{i-1/2}^{n+1/2} h_{i-1/2}^{n+1/2}). \quad (9)$$

84 To calculate  $u_{i\pm 1/2}^{n+1/2}$  first  $u$  is advanced in time by  $\mathcal{G}_u$  then using linear interpolation in both space and time gives

$$85 \quad u_{i+1/2}^{n+1/2} = \frac{u_{i+1}^{n+1} + u_{i+1}^n + u_i^{n+1} + u_i^n}{4}, \quad (10)$$

$$86 \quad u_{i-1/2}^{n+1/2} = \frac{u_i^n + u_i^{n+1} + u_{i-1}^{n+1} + u_{i-1}^n}{4}. \quad (11)$$

87 Thus we have the following update scheme

$$88 \quad \begin{bmatrix} \mathbf{h}^{n+1} \\ \mathbf{u}^{n+1} \end{bmatrix} = \mathcal{E}(\mathbf{u}^n, \mathbf{h}^n, \mathbf{u}^{n-1}, \mathbf{h}^{n-1}, \Delta x, \Delta t). \quad (12)$$

### 89    Second Order Naive Finite Difference Method

90    Here we also present a completely naive method for comparative purposes, to do this  
 91 we apply the procedure used above on (1b) to (1a). Thus the derivatives were first ex-  
 92 panded then approximated by second order centered finite differences after rearranging  
 this to give an update formula we obtain

$$93 \quad h_i^{n+1} = h_i^{n-1} - \Delta t \left( u_i^n \frac{h_{i+1}^n - h_{i-1}^n}{\Delta x} + h_i^n \frac{u_{i+1}^n - u_{i-1}^n}{\Delta x} \right). \quad (13)$$

94    Preforming this update for all  $i$  will be denoted by  $\mathcal{G}_h(\mathbf{u}^n, \mathbf{h}^n, \mathbf{h}^{n-1}, \Delta x, \Delta t)$ . Thus we get  
 95 the naive second-order centred finite difference method for the Serre equations

$$96 \quad \begin{aligned} \mathbf{h}^{n+1} &= \mathcal{G}_h(\mathbf{u}^n, \mathbf{h}^n, \Delta x, \Delta t) \\ \mathbf{u}^{n+1} &= \mathcal{G}_u(\mathbf{u}^n, \mathbf{h}^n, \mathbf{u}^{n-1}, \mathbf{h}^{n-1}, \Delta x, \Delta t) \end{aligned} \quad \left\{ \mathcal{G}(\mathbf{u}^n, \mathbf{h}^n, \mathbf{u}^{n-1}, \mathbf{h}^{n-1}, \Delta x, \Delta t) \right\}. \quad (14)$$

100 **CONSERVATIVE FORM OF THE SERRE EQUATIONS**

101 To overcome the aforementioned difficulty of mixed derivatives the Serre equations (1)  
102 can be reformulated into conservative form. This is accomplished by the introduction of a  
103 new quantity (Le Métayer et al. 2010; Zoppou 2014)

104 
$$G = uh - h^2 \frac{\partial h}{\partial x} \frac{\partial u}{\partial x} - \frac{h^3}{3} \frac{\partial^2 u}{\partial x^2}. \quad (15)$$

105 Consequently, (1) can be rewritten as

106 
$$\frac{\partial h}{\partial t} + \frac{\partial(uh)}{\partial x} = 0 \quad (16a)$$

107 and

108 
$$\frac{\partial G}{\partial t} + \frac{\partial}{\partial x} \left( Gu + \frac{gh^2}{2} - \frac{2h^3}{3} \frac{\partial u}{\partial x} \frac{\partial u}{\partial x} \right) = 0. \quad (16b)$$

109

110 **A Hybrid Finite Difference-Volume Method for Serre Equations in Conservative**  
111 **Form**

112 The conservative form (16) allows for a wider range of numerical techniques such  
113 as finite element methods (Li et al. 2014) and finite volume methods (Le Métayer et al.  
114 2010; Zoppou 2014). In this paper the first ( $\mathcal{V}_1$ ), second ( $\mathcal{V}_2$ ) and third-order ( $\mathcal{V}_3$ ) finite  
115 difference-volume methods (FDVM) of [] will be used. These have been validated and  
116 their order of accuracy confirmed.

117 **Stability Condition**

118 To ensure stability of the FDVMs the time-step  $\Delta t$  must satisfy the Courant-Friedrichs-  
119 Lewy (CFL) criteria (A. Harten 1983)

$$\Delta t < \frac{Cr\Delta x}{2 \max \{|\lambda|\}} \quad (17)$$

120 with  $0 < Cr \leq 1$  where  $\lambda$  is the wave speed. For the Serre equations it has been  
121 demonstrated that the wave speed is bounded by the wave speed of the Shallow Water  
122 Wave equations.[zoppou]

123 **NUMERICAL SIMULATIONS**

124 In this section the methods introduced in this paper will be validated by using them  
125 to approximate an analytic solution of the Serre equations, this will also be used to verify

their order of accuracy. Then an in depth comparison of these methods for a smooth approximation to the discontinuous dam break problem will be provided to investigate the behaviour of these equations in the presence of discontinuities. This is a problem that so far has only received a proper treatment in (El et al. 2006), with other research giving only a cursory investigation into the topic.

## SOLITON

Currently cnoidal waves are the only family of analytic solutions to the Serre equations (Carter and Cienfuegos 2011). Solitons are a particular instance of cnoidal waves that travel without deformation and have been used to verify the convergence rates of the described methods in this paper.

For the Serre equations the solitons have the following form

$$h(x, t) = a_0 + a_1 \operatorname{sech}^2(\kappa(x - ct)), \quad (18a)$$

142

$$u(x, t) = c \left( 1 - \frac{a_0}{h(x, t)} \right), \quad (18b)$$

143

144

145

$$\kappa = \frac{\sqrt{3a_1}}{2a_0 \sqrt{a_0 + a_1}} \quad (18c)$$

146 and

$$c = \sqrt{g(a_0 + a_1)} \quad (18d)$$

151 where  $a_0$  and  $a_1$  are input parameters that determine the depth of the quiescent water and  
 152 the maximum height of the soliton above that respectively. In the simulation  $a_0 = 1\text{m}$ ,  $a_1 =$   
 153  $1\text{m}$  for  $x \in [-50\text{m}, 250\text{m}]$  and  $t \in [0\text{s}, 50\text{s}]$ . With  $\Delta t = 0.5\lambda^{-1}\Delta x$  where  $\lambda = \sqrt{g(a_0 + a_1)}$   
 154 which is the maximum wave speed, this satisfies the CFL condition (17).

## Results

155 This numerical experiment and its results for the FDVM have been reported by [], this  
 156 paper only reports the results for the two finite difference methods  $\mathcal{G}$  and  $\mathcal{E}$ .

158 From Figure 2(a) it can be seen that  $\mathcal{G}$  both  $\mathcal{E}$  accurately model the highly non-linear  
 159 soliton problem reproducing the analytic solution up to graphical accuracy with the same  
 160  $\Delta t$  and  $\Delta x$  as in []. This demonstrates that for smooth problems both the FD and FDVM  
 161 are comparable when using similar spatial and temporal resolutions.

162 To demonstrate that in fact  $\mathcal{E}$  and  $\mathcal{G}$  are consistent three measures were used. the first  
 163 measures the relative distance of the numerical results in both  $h$  and  $u$  from the analytic

164 solution and is defined for a general quantity  $q$  and an approximation to it  $q^*$  at  $n$  values  
 165 like so

$$L_1 = \frac{\sum_{i=0}^n |q_i - q_i^*|}{\sum_{i=0}^n |q_i|}. \quad (19)$$

The second measures how well the schemes conserve mass and momentum with

$$C_1 = \frac{|C_q(0) - C_{q^*}(t_f)|}{|C_q(0)|} \quad (20)$$

where  $t_f$  is the final time of the numerical experiment. For  $C_q(0)$  the analytic value is used while a numerical calculation is used for  $C_{q^*}(t_f)$  which for second-order methods is equivalent to taking the sum of all the  $q_i$ 's and then multiplying by  $\Delta x$ . Lastly how well the scheme conserves the Hamiltonian of the Serre equations is measured by

$$H_1 = \frac{|\mathcal{H}(0) - \mathcal{H}(t_f)|}{|\mathcal{H}(0)|} \quad (21)$$

166 where  $t_f$  is the final time of the numerical experiment. For  $\mathcal{H}(0)$  the analytic value is used  
 167 while a numerical calculation is used for  $\mathcal{H}(t_f)$ .

168 From Figure 3 it can be seen that both FD methods are convergent under  $L_1$  with  
 169 second-order accuracy. In both  $L_1$  plots the round-off effects for very small  $\Delta x$  can be ob-  
 170 served resulting in a loss of accuracy. For Figure 3(c) the effects of large  $\Delta x$ 's can be seen  
 171 which is a suboptimal rate of convergence as the initial conditions cannot be accurately  
 172 represented by the discretisation.

173  $H_1$  measures how well the method conserves the Hamiltonian, from Figures 3(b) and  
 174 3(d) we see that the FD methods conserve the Hamiltonian well and converge to the correct  
 175 value of 0 for  $H_1$ . Unfortunately, the point at which round off errors dominate is much  
 176 earlier than for  $L_1$  this is because the  $H_1$  uses a very high order numerical integration  
 177 calculation requiring more calculations than  $L_1$  introducing more round off errors.  $H_1$   
 178 also suffers from the same problems that  $C_1$  suffers as well leading to the stagnation of  
 179 convergence seen in both. Although we do attain similar order of magnitudes for  $L_1$  and  
 180  $H_1$  before round off errors dominate. []

181 Lastly Figure 4 demonstrates conservation of both mass and momentum to at least  
 182 second-order for both FD schemes. Both schemes conserve mass very well with round off  
 183 error dominance occurring at the same place as for  $L_1$ . Momentum has the appropriate  
 184 order of accuracy for larger  $\Delta x$  but then stagnates as  $\Delta x$  decreases. This is due to the use  
 185 of a finite difference method which is not necessarily conservative on (1b) which is not

186 in conservation law form leading to poor conservation of the momentum variable as com-  
 187 pared to mass. Figure 4 however still demonstrates that these schemes are still relatively  
 188 conservative and certainly there is not some drastic change in the momentum and mass in  
 189 a system using these methods.

190 These results demonstrate that these methods solve the Serre equations well and as  
 191 such are appropriate to solve problems with smooth initial conditions. Because these meth-  
 192 ods do not require a reformulation, an elliptic solver or a bound on the wave speed these  
 193 methods demonstrate that these added complexities are not the cause of the behaviours  
 194 observed for the smooth dam break problem. Thus the observed behaviours are a property  
 195 of the underlying equations and not the result of a particular numerical technique.

## 196 SMOOTHED DAM-BREAK

197 The discontinuous dam-break problem can be approximated smoothly using the hy-  
 198 perbolic tangent function. Such an approximation will be called a smoothed dam-break  
 199 problem and will be defined as such

$$200 \quad h(x, 0) = h_0 + \frac{h_1 - h_0}{2} (1 + \tanh(\alpha(x_0 - x))), \quad (22a)$$

202

$$203 \quad u(x, 0) = 0.0m/s. \quad (22b)$$

205 Where  $\alpha$  is given and controls the width of the transition between the two dam-break  
 206 heights of  $h_0$  and  $h_1$ . For large  $\alpha$  the width is small and vice versa. We measure the  
 207 transition width by taking the width of the dam break problem inside which 90% of the  
 208 transition between the two states occurs which will be referred to as  $\beta$ .  $\beta$  has the following  
 209 formula independent of  $h_0$ ,  $h_1$  and  $x_0$

$$210 \quad \beta = \frac{2 \tanh^{-1}(0.9)}{\alpha}. \quad (23)$$

212

213 The dam break problem for the one dimensional Serre equations was analysed by El  
 214 et al. (2006) and an expression for the lead soliton amplitude of a bore was given as

$$215 \quad \frac{\Delta}{(a^+ + 1)^{1/4}} - \left( \frac{3}{4 - \sqrt{a^+ + 1}} \right)^{21/10} \left( \frac{2}{1 + \sqrt{a^+ + 1}} \right)^{2/5} = 0 \quad (24)$$

217 where  $\Delta = h_1/h_0$  and  $a^+$  is the leading soliton amplitude. This measure will be used to  
 218 verify that our results are sensible although as pointed out by El et al. (2006)  $a^+$  and the  
 219 measured lead soliton amplitude of a numerical solution can differ.

220 In the first series of experiments  $h_0 = 1.0m$ ,  $h_1 = 1.8m$  on  $x \in [0m, 1000m]$  for  
 221  $t \in [0s, 30s]$  with  $x_0 = 500m$ . This scenario replicates one presented by El et al. (2006)  
 222 and Le Métayer et al. (2010) and as such serves as a comparison for the results of both  
 223 with  $\mathcal{E}$  and  $\mathcal{G}$  and the 3 different order FDVMs described in []. The simulations were run  
 224 with various values of  $\Delta x$  and  $\beta$ . To ensure stability, especially of both FD methods a very  
 225 restrictive relation of  $\Delta t = 0.01\Delta x$  was chosen. For  $\mathcal{V}_2$   $\theta = 1.2$ . From this description we  
 226 calculate the Hamiltonian at the initial time analytically

$$\mathcal{H}(0) = 10398.6 - 0.7848 \times \left[ \frac{2}{\alpha} \tanh(500\alpha) \right], \quad (25)$$

227 which will be used to verify the produced numerical results. Applying (24) with analytic  
 228 results of [] gives  $\Delta = 1.36898$  for the bore and thus  $a^+ = 1.73640$  (5 decimal places).

229 Figure 5 shows the initial water profiles of smooth dam break problems with various  $\beta$   
 230 values. It also indicates what the 90% of the transition width for  $\beta = 117.778$  is, with 90%  
 231 capturing most of the transition.

232 The following is an investigation into the results beginning with the behaviours of the  
 233 solutions as  $\Delta x \rightarrow 0$ .

### 234 **Changing $\Delta x$**

235 Decreasing  $\Delta x$  allows the numerical method to better approximate the analytic solution  
 236 to the equations. So for our validated numerical methods it would be expected that smaller  
 237  $\Delta x$ 's provide a closer approximation to the analytic solution.

238 In this comparison we pick an  $\beta$  and a method and investigate the result of decreasing  
 239  $\Delta x$ . Because the smoothness of the initial conditions depends on both  $\Delta x$  and  $\beta$  one must  
 240 be careful that the initial conditions are sufficiently smooth as  $\Delta x$  is decreased. This is of  
 241 particular importance for the two finite difference methods as they do not correctly handle  
 242 discontinuous initial conditions.

243 The first and most important observation is that there are four types of behaviour as  
 244  $\Delta x \rightarrow 0$  depending on the  $\beta$  and the numerical method. The four scenarios are identified  
 245 by the behaviour of the solutions when  $\Delta x$  is small and they correspond to different results  
 246 in the literature. For brevity the only examples of these scenarios will the solutions of  $\mathcal{V}_3$   
 247 although they all occurred for  $\mathcal{V}_2$ ,  $\mathcal{E}$  and  $\mathcal{G}$  but not  $\mathcal{V}_1$  which was too diffusive.

248 The first behaviour which will be referred to as the non-oscillatory scenario has such  
 249 smooth initial conditions that no oscillations were introduced by  $t = 30s$ , although given  
 250 sufficient time an undular bore would develop. An example of this behaviour was seen  
 251 at  $\beta = 117.778$  in Figure 6. Because this is a very smooth problem we observe rapid  
 252 convergence with all the numerical results being graphically identical. This scenario re-

253 sembles very diffusive solutions of the shallow water wave equations in that it contains  
254 only a rarefaction and a shock with no dispersive waves.

255 This convergence is also present in Figure 7 with both the  $L_1$  and  $H_1$  measures. Al-  
256 though now  $L_1$  uses the solution of the smallest  $\Delta x$  as an approximation to the analytic  
257 solution as none exists for this problem. In both measures the order of accuracy is the  
258 theoretical one, with round-off errors becoming dominant below  $\Delta x = 0.1$ .

259 The second scenario will be referred to as the flat scenario due to the presence of a  
260 constant height state between the oscillations at the shock and rarefaction fan. An example  
261 of the numerical results for this scenario can be seen in Figure 8 when  $\beta = 5.8889$ . This  
262 scenario corresponds to the results presented by Le Métayer et al. (2010) and Mitsotakis  
263 et al. (2014).

264 As  $\Delta x$  decreases the solutions converge which is sensible since for the  $\Delta x$  in Figure  
265 8 the initial conditions are smooth as can be seen in Figure 5 and these methods have  
266 been verified for smooth problems. So that by  $\Delta x = 10/2^8$  the solutions for higher  $\Delta x$  are  
267 visually identical.

268 The measures  $L_1$  and  $H_1$  also demonstrate good convergence with the expected order  
269 of convergence in the middle of the plot. Suboptimal convergence is expected for large  $\Delta x$   
270 as the problem is not properly discretised to resolve the oscillations and so both  $H_1$  and  
271  $L_1$  suffer. For small  $\Delta x$   $H_1$  becomes suboptimal suggesting significant round-off errors,  
272 however this effect is masked by  $L_1$  because the smallest  $\Delta x$  is has no comparsion and  
273 because it is based on comparison of two numerical simulations and not the analy

274 For the results in Figure 8 the Hamiltonian for this problem is 10395.4608(units). The  
275 relative error for the conservation of the Hamiltonian by the third order method with  $\Delta x =$   
276  $10/2^{10}$  was  $9.77469897234 \times 10^{-6}$ . This low relative error suggests that our numerical  
277 method is solving the equations appropriately validating our results. We are however  
278 seeing the trend that will continue further on that our relative error is increasing as we  
279 better approximate the discontinuous initial conditions of the dam break problem.

280 The third scenario will be referred to as the contact discontinuity scenario due to the  
281 use of that term to describe it by El et al. (2006). For the higher-order methods it occurs at  
282  $\alpha = 2.5$  and so far has not occurred for the first order method[ ]. The contact discontinuity  
283 scenarios main feature is that the oscillations from the rarefaction fan and the shock decay  
284 and appear to meet at a point as can be seen in Figure 10. For the experiments performed  
285 this doesn't appear to be an actual centre point but rather that the oscillations decay so  
286 quickly around the 'contact discontinuity' that it appears to be the case. All the higher  
287 order methods so far have not shown a converged solution as  $\Delta x$  decreases. However it  
288 does appear that convergence is likely with the solutions getting closer together.

289 For the results in Figure 10 the Hamiltonian of the initial conditions was calculated nu-  
290 merically to be 10397.97216(units). The relative error for the conservation of the Hamil-

tonian by the third order method with  $\Delta x = 10/2^{10}$  was  $9.74612149745 \times 10^{-6}$ . This shows that we are still accurately capturing the behaviour of the equations validating the of El et al. (2006).

The fourth scenario will be referred to as the bump scenario due to the oscillations no longer decaying down towards a point but rather growing around where the contact discontinuity was in the previous scenario as can be seen in Figure 12. This behaviour has hitherto not been published and is certainly not an expected result. There are some important observations. Firstly changing  $\alpha$  increases the height of the bump for the lowest resolution methods although after [] increasing  $\alpha$  has no effect[huh?]. The behaviour of these solutions in Figure 12 do not clearly show convergence.

For the results in Figure 12 the Hamiltonian of the initial conditions was calculated numerically to be 10398.5984304(units). The relative error for the conservation of the Hamiltonian by the third order method with  $\Delta x = 10/2^{10}$  was  $1.79088558176 \times 10^{-6}$ . This shows that we are still accurately capturing the behaviour of the equations validating the of El et al. (2006).

All of the scenarios described above and displayed using the higher-order FDVM also occur for the FDM, however because finite differences cannot properly handle discontinuities this is a little more subtle. Firstly, since for each  $\alpha$  there is a  $\Delta x$  such that for larger  $\Delta x$  the smooth dam break problem is no longer smooth enough for a finite difference approximation to be appropriate. This becomes a problem for the contact discontinuity and bump scenarios since they require higher  $\alpha$  and are thus are not very smooth to begin with. The result of this are non-physical looking oscillations for large  $\Delta x$  values that were not replicated by the FDVM and thus can be attributed to this flaw of FDM as in Figure ??.

Overall there where two types of trending behaviours as  $\Delta x$  was decreased one for the FDM and another for the FDVM. FDM decreased the number of oscillations in the solution as in Figure [], while FDVM increased the number of oscillations in the solution as can be seen in Figure []. This is explained by Zoppou and Roberts (1996) as the FDM are second order finite difference approximations their errors are dissipative thus introducing oscillatory errors which are most prominent when  $\Delta x$  and therefore the errors are large. While the behaviour of the FDVM is explained by a series of effects [] [TVD, treating things as cell averages, thus flattening things in cells,].

### 322 **Changing $\alpha$**

Increasing  $\alpha$  allows the initial conditions (7) to approach the dam break problem with  $h_1$  to the left and  $h_0$  to the right centred around  $x_0$ . So it would be expected that as  $\alpha \rightarrow \infty$  that the solution of the smooth dam break problem would approach the corresponding dam break problem. This is the case for numerical methods because for a fixed  $\Delta x$   $\alpha$  can be chosen large enough that (7) is precisely the dam break problem. This can be seen in Figure [] with  $\Delta x =$  where the required  $\alpha$  for this to occur is below 1000 which was

329 the maximum  $\alpha$  value used in these experiments. However, only the FDVM were able to  
330 handle such large  $\alpha$ 's because the initial conditions are not smooth enough to allow for  
331 stability in the FDM as can be seen in Figure []. While the FDVM handled this quite well  
332 and for all  $\Delta x$  tested as  $\alpha$  increased the solutions converged, even though for higher  $\Delta x$  []  
333  $\alpha$  was not large enough to make (7) a jump discontinuity.

334 This confirms the superiority of the FDVM to handle non smooth initial conditions and  
335 the inability of FDM to handle them. Even near discontinuous initial conditions caused  
336 problems for the FDM with the introduction of oscillations that were not replicated by  
337 the FDVM and appeared to be non-physical. An example of these transitional solutions  
338 between the properly smooth initial conditions and the unstable discontinuous ones can be  
339 seen in Figure []. [](only compare the models when FD started smooth enough)

340 For the range of  $\alpha$ 's which are smooth enough for the FDM to be appropriate then as  
341  $\alpha$  increases the number of oscillations increases as well for both the FDM and the FDVM.  
342 So that the smoothness of the initial conditions controls the oscillations but this depends  
343 on  $\Delta x$  since for a fixed  $\alpha$  the smoothness of the discretised initial conditions depends on  
344  $\Delta x$ . [] (relative smoothness, more universal number)

345 It was observed that  $\Delta x$  can be chosen large enough such that increasing  $\alpha$  does not  
346 resolve some of the more complex structure observed for smaller  $\Delta x$  values. This  $\Delta x$   
347 depends on the model most notably for the first-order finite difference-volume scheme this  
348  $\Delta x$  is very small. An example of this for the third-order FDVM scheme can be seen in  
349 Figure [].

### 350 **Comparison of Models**

351 The first-order FDVM was too diffuse and

### 352 **Source**

### 353 **CONCLUSIONS**

### 354 **ACKNOWLEDGEMENTS**

### 355 **REFERENCES**

- 356 A. Harten, A. (1983). "High resolution schemes for hyperbolic conservation laws." *Journal*  
357 *of Computational Physics*, 49(3), 357–393.
- 358 Carter, J. D. and Cienfuegos, R. (2011). "Solitary and cnoidal wave solutions of the Serre  
359 equations and their stability." *European Journal of Mechanics B/Fluids*, 30(3), 259–268.
- 360 El, G., Grimshaw, R. H. J., and Smyth, N. F. (2006). "Unsteady undular bores in fully  
361 nonlinear shallow-water theory." *Physics of Fluids*, 18(027104).
- 362 Green, A. E. and Naghdi, P. M. (1976). "A derivation of equations for wave propagation  
363 in water of variable depth." *Journal of Fluid Mechanics*, 78(2), 237–246.
- 364 Lannes, D. and Bonneton, P. (2009)." *Physics of Fluids*, 21(1), 16601–16610.

- 365 Le Métayer, O., Gavrilyuk, S., and Hank, S. (2010). “A numerical scheme for the Green-  
366 Naghdi model.” *Journal of Computational Physics*, 229(6), 2034–2045.
- 367 Li, M., Guyenne, P., Li, F., and Xu, L. (2014). “High order well-balanced CDG-FE meth-  
368 ods for shallow water waves by a Green-Naghdi model.” *Journal of Computational  
369 Physics*, 257, 169–192.
- 370 Li, Y. A. (2002). “Hamiltonian Structure and Linear Stability of Solitary Waves of the  
371 Green-Naghdi Equations.” *Journal of Nonlinear Mathematical Physics*, 9, 99–105.
- 372 Mitsotakis, D., Dutykh, D., and Carter, J. (2014). “On the nonlinear dynamics of the  
373 traveling-wave solutions of the serre equations.” *arXiv preprint arXiv:1404.6725*.
- 374 Su, C. H. and Gardner, C. S. (1969). “Korteweg-de Vries equation and generalisations.  
375 III. Derivation of the Korteweg-de Vries equation and Burgers equation.” *Journal of  
376 Mathematical Physics*, 10(3), 536–539.
- 377 Zoppou, C. (2014). “Numerical solution of the One-dimensional and Cylindrical Serre  
378 Equations for Rapidly Varying Free Surface Flows.” Ph.D. thesis, Australian National  
379 University, Australian National University.
- 380 Zoppou, C. and Roberts, S. (1996). “Behaviour of finite difference schemes for advection  
381 diffusion equations.” *Technical Report Mathematics Research Report No.MRR 062-96*.

382 **List of Figures**

383 1	The notation used for one-dimensional flow governed by the Serre equation.	16
384 2	Water profile for the soliton problem (6) for $\mathcal{G}$ ((a),(b)) and $\mathcal{E}$ ((c),(d)) when $\Delta x = 10/2^{12}$ with the initial conditions (—), analytic solution (—) and numerical result (●). . . . .	17
387 3	On the left $L_1$ errors for $h$ ( $\Delta$ ) and $u$ ( $\square$ ) and on the right $H_1$ ( $\circ$ ) for the soliton problem with (a) and (b) for $\mathcal{G}$ and (c) and (d) for $\mathcal{E}$ . . . . .	18
389 4	$C_1$ for $h$ ( $\Delta$ ) and $uh$ ( $\diamond$ ) for numerical solutions $\mathcal{G}$ (a) and $\mathcal{E}$ (b) of the soliton problem. . . . .	19
391 5	Initial conditions for the smooth dambreak problem with $\beta = 0.294$ (—), $\beta = 1.17778$ (—), $\beta = 5.8888$ (—) and $\beta = 117.778$ (—) with reference $\beta$ interval(— —). . . . .	20
394 6	Numerical results of $\mathcal{V}_3$ at $t = 30s$ for the smooth dam break problem with $\beta = 117.778$ for $\Delta x = 10/2^{10}$ (—), $\Delta x = 10/2^9$ (—), $\Delta x = 10/2^8$ (—), $\Delta x = 10/2^7$ (—), $\Delta x = 10/2^6$ (—), $\Delta x = 10/2^5$ (—), $\Delta x = 10/2^4$ (—) with reference value $a^+$ (— —). . . . .	21
398 7	$L_1$ for $h$ ( $\Delta$ ) and $u$ ( $\square$ ) and $H_1$ ( $\circ$ ) for $\mathcal{V}_3$ 's solution for the smooth dambreak problem with $\beta = 117.778$ . . . . .	22
400 8	Numerical results of $\mathcal{V}_3$ at $t = 30s$ for the smooth dam break problem with $\beta = 5.8888$ for $\Delta x = 10/2^{10}$ (—), $\Delta x = 10/2^9$ (—), $\Delta x = 10/2^8$ (—), $\Delta x = 10/2^7$ (—), $\Delta x = 10/2^6$ (—), $\Delta x = 10/2^5$ (—), $\Delta x = 10/2^4$ (—) with reference value $a^+$ (— —). . . . .	23
404 9	$L_1$ for $h$ ( $\Delta$ ) and $u$ ( $\square$ ) and $H_1$ ( $\circ$ ) for $\mathcal{V}_3$ 's solution for the smooth dambreak problem with $\beta = 5.8888$ . . . . .	24
406 10	Numerical results of $\mathcal{V}_3$ at $t = 30s$ for the smooth dam break problem with $\beta = 1.17778$ for $\Delta x = 10/2^{10}$ (—), $\Delta x = 10/2^9$ (—), $\Delta x = 10/2^8$ (—), $\Delta x = 10/2^7$ (—), $\Delta x = 10/2^6$ (—), $\Delta x = 10/2^5$ (—), $\Delta x = 10/2^4$ (—) with reference value $a^+$ (— —). . . . .	25
410 11	$L_1^*$ for $h$ ( $\Delta$ ) and $u$ ( $\square$ ) and $H_1$ ( $\circ$ ) for $\mathcal{V}_3$ 's solution for the smooth dambreak problem with $\beta = 1.17778$ . . . . .	26
412 12	Numerical results of $\mathcal{V}_3$ at $t = 30s$ for the smooth dam break problem with $\beta = 0.294$ for $\Delta x = 10/2^{10}$ (—), $\Delta x = 10/2^9$ (—), $\Delta x = 10/2^8$ (—), $\Delta x = 10/2^7$ (—), $\Delta x = 10/2^6$ (—), $\Delta x = 10/2^5$ (—), $\Delta x = 10/2^4$ (—) with reference value $a^+$ (— —). . . . .	27
416 13	$L_1^*$ for $h$ ( $\Delta$ ) and $u$ ( $\square$ ) and $H_1$ ( $\circ$ ) for $\mathcal{V}_3$ 's solution for the smooth dambreak problem with $\beta = 0.294$ . . . . .	28

418	14	$H_1$ for $\mathcal{V}_3$ (a) and $\mathcal{G}$ 's (b) solution for the smooth dambreak problem at $t = 30s$ with $\beta = 0.294$ demonstrating when $\mathcal{H}(0s) \geq \mathcal{H}(30s)$ (○) and $\mathcal{H}(0s) < \mathcal{H}(30s)$ (●). . . . .	29
419			
420	15	Numerical results of $\mathcal{G}$ at $t = 30s$ for the smooth dam break problem with $\beta = 5.8888$ for $\Delta x = 10/2^4$ (—), $\Delta x = 10/2^5$ (—), $\Delta x = 10/2^6$ (—), $\Delta x = 10/2^7$ (—), $\Delta x = 10/2^8$ (—), $\Delta x = 10/2^9$ (—), $\Delta x = 10/2^{10}$ (—) with reference value $a^+$ (— —) . . . . .	30
421			
422	16	Numerical results of $\mathcal{G}$ at $t = 30s$ for the smooth dam break problem with $\beta = 0.294$ for $\Delta x = 10/2^7$ (—), $\Delta x = 10/2^8$ (—), $\Delta x = 10/2^9$ (—), $\Delta x = 10/2^{10}$ (—) with reference value $a^+$ (— —) . . . . .	31
423			
424	17	Smooth dam break problem at $t = 100s$ for $\mathcal{V}_3$ with $\beta = 0.294$ for $\Delta x = 10/2^{10}$ (—) with reference value $a^+$ (— —). . . . .	32
425			
426	18	Lead soliton height plotted over time for the smooth dam break problem at $t = 100s$ for $\mathcal{V}_3$ with $\beta = 0.294$ for $\Delta x = 10/2^{10}$ (—) with reference value $a^+$ (— —). . . . .	33
427			
428	19	Numerical results of $\mathcal{V}_3$ at $t = 100s$ for the smooth dam break rarefaction fan for $\Delta x = 10/2^{10}$ with $\beta = 0.2944$ (—), $\beta = 0.3464$ (—), $\beta = 0.4530$ (—), $\beta = 0.6543$ (—) and $\beta = 1.1778$ (—) and $\beta = 5.8888$ (—). . . . .	34
429			
430	20	Numerical results of $\mathcal{V}_3$ at $t = 100s$ for the smooth dam break shock wave for $\Delta x = 10/2^{10}$ with $\beta = 0.2944$ (—), $\beta = 0.3464$ (—), $\beta = 0.4530$ (—), $\beta = 0.6543$ (—) and $\beta = 1.1778$ (—) and $\beta = 5.8888$ (—). . . . .	35
431			
432	21	Numerical results of $\mathcal{V}_3$ at $t = 100s$ for the smooth dam break $\beta = 0.2944$ (—) and the smooth dam break shock wave (—), $\beta = 0.2944$ for $\Delta x = 10/2^{10}$ . . . . .	36
433			
434	22	Numerical results of $\mathcal{V}_3$ at $t = 100s$ for the smooth dam break $\beta = 0.2944$ (—) and the smooth dam break shock wave $\beta = 0.2944$ (—) for $\Delta x = 10/2^{10}$ . . . . .	37
435			
436	23	$\mathcal{H}_1$ for $\mathcal{V}_3$ solution of the smooth dam break with $\beta = 0.2944$ and $\Delta x = 10/2^{10}$ at $t = 0s$ (—) and $t = 100s$ (—). . . . .	38
437			
438	24	$\mathcal{H}_2$ for $\mathcal{V}_3$ solution of the smooth dam break with $\beta = 0.2944$ and $\Delta x = 10/2^{10}$ at $t = 0s$ (—) and $t = 100s$ (—). . . . .	39
439			
440	25	$\mathcal{H}_3$ for $\mathcal{V}_3$ solution of the smooth dam break with $\beta = 0.2944$ and $\Delta x = 10/2^{10}$ at $t = 0s$ (—) and $t = 100s$ (—). . . . .	40
441			
442	26	Proportion of $\mathcal{H}$ made up by $\mathcal{H}_1$ (—), $\mathcal{H}_2$ (—) and $\mathcal{H}_3$ (—) for $\mathcal{V}_3$ solution of the smooth dam break with $\beta = 0.2944$ and $\Delta x = 10/2^{10}$ over time. . . . .	41
443			
444	27	$h$ (—) and adjusted $u$ (—) for $\mathcal{V}_3$ solution of the smooth dam break with $\beta = 0.2944$ and $\Delta x = 10/2^{10}$ at $t = 100s$ . . . . .	42
445			
446	28	$v_{DB}$ (—) and $v_{CD}$ (○) for $\mathcal{V}_3$ solution of the various smooth dam break problems with $\beta = 0.2944$ and $\Delta x = 10/2^{10}$ at $t = 100s$ . . . . .	43
447			
448			
449			
450			
451			
452			
453			
454			
455			

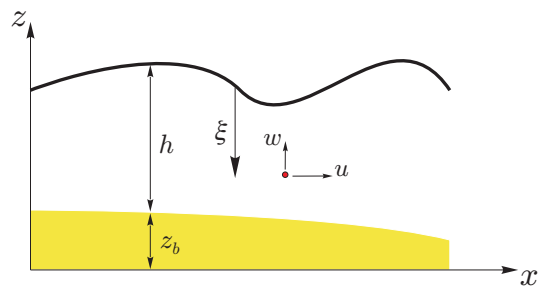


FIG. 1: The notation used for one-dimensional flow governed by the Serre equation.

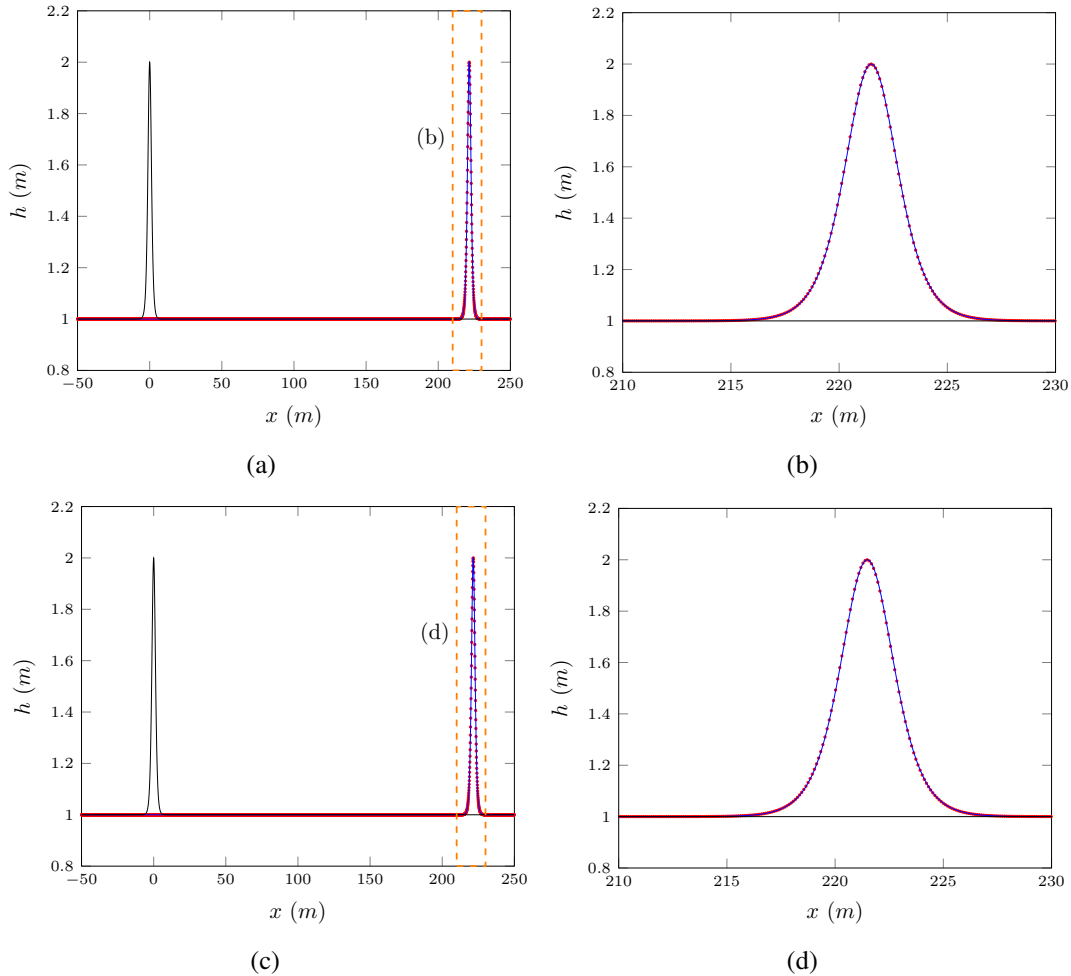


FIG. 2: Water profile for the soliton problem (6) for  $\mathcal{G}$  ((a),(b)) and  $\mathcal{E}$  ((c),(d)) when  $\Delta x = 10/2^{12}$  with the initial conditions (—), analytic solution (—) and numerical result (•).

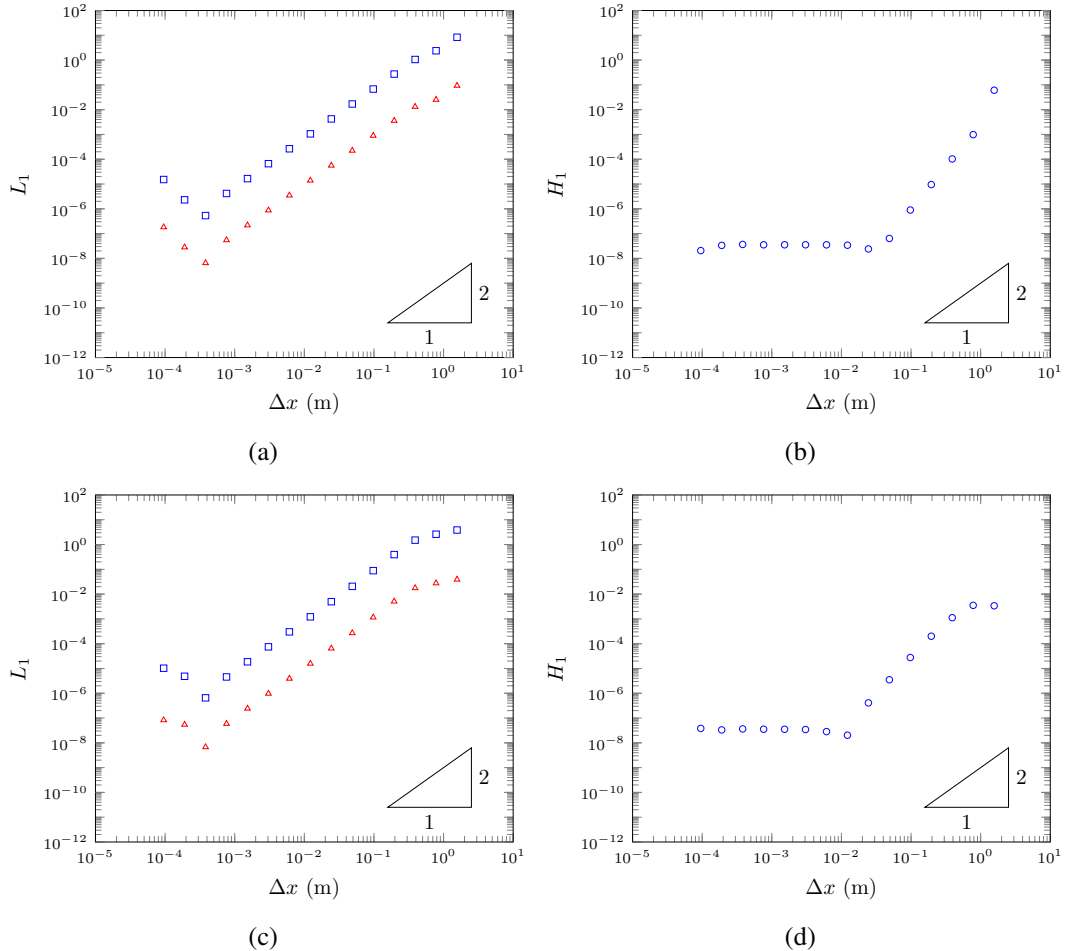


FIG. 3: On the left  $L_1$  errors for  $h$  ( $\triangle$ ) and  $u$  ( $\square$ ) and on the right  $H_1$  ( $\circ$ ) for the soliton problem with (a) and (b) for  $\mathcal{G}$  and (c) and (d) for  $\mathcal{E}$ .

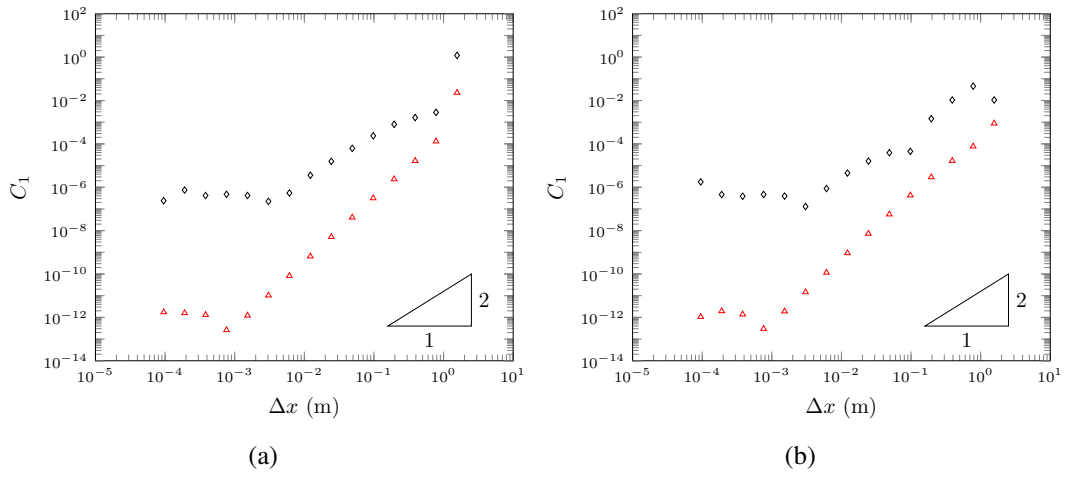


FIG. 4:  $C_1$  for  $h$  ( $\Delta$ ) and  $uh$  ( $\diamond$ ) for numerical solutions  $\mathcal{G}$  (a) and  $\mathcal{E}$  (b) of the soliton problem.

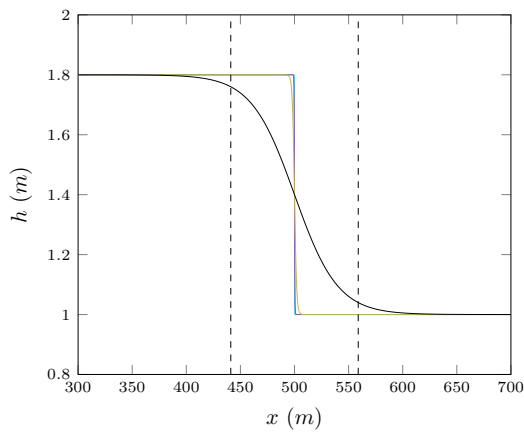
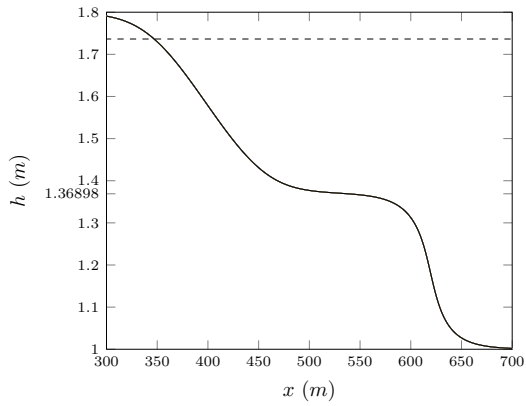


FIG. 5: Initial conditions for the smooth dambreak problem with  $\beta = 0.294$  (—),  $\beta = 1.17778$  (—),  $\beta = 5.8888$  (—) and  $\beta = 117.778$  (—) with reference  $\beta$  interval(— —).



(a)

FIG. 6: Numerical results of  $\mathcal{V}_3$  at  $t = 30s$  for the smooth dam break problem with  $\beta = 117.778$  for  $\Delta x = 10/2^{10}$  (—),  $\Delta x = 10/2^9$  (—),  $\Delta x = 10/2^8$  (—),  $\Delta x = 10/2^7$  (—),  $\Delta x = 10/2^6$  (—),  $\Delta x = 10/2^5$  (—),  $\Delta x = 10/2^4$  (—) with reference value  $a^+$  (— —).

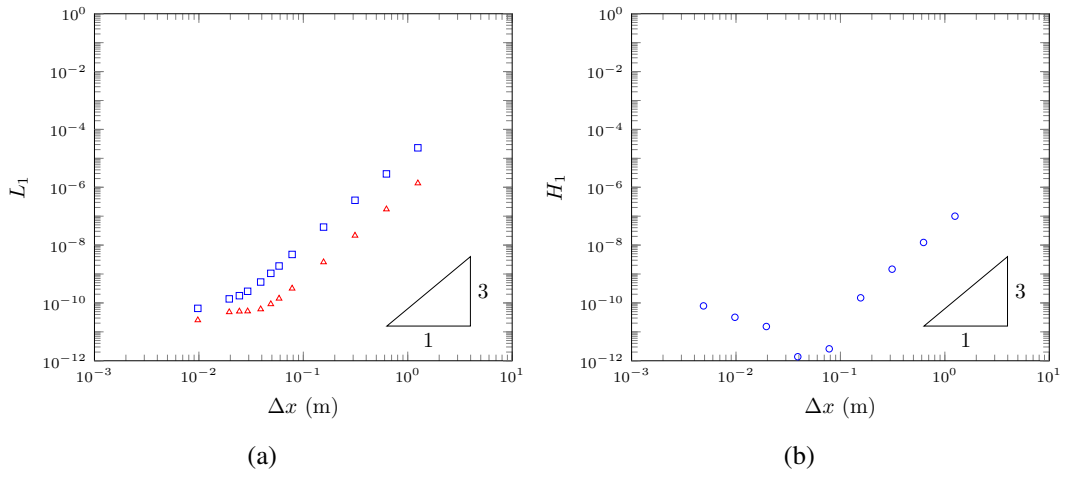


FIG. 7:  $L_1$  for  $h$  ( $\triangle$ ) and  $u$  ( $\square$ ) and  $H_1$  ( $\circ$ ) for  $\mathcal{V}_3$ 's solution for the smooth dambreak problem with  $\beta = 117.778$ .

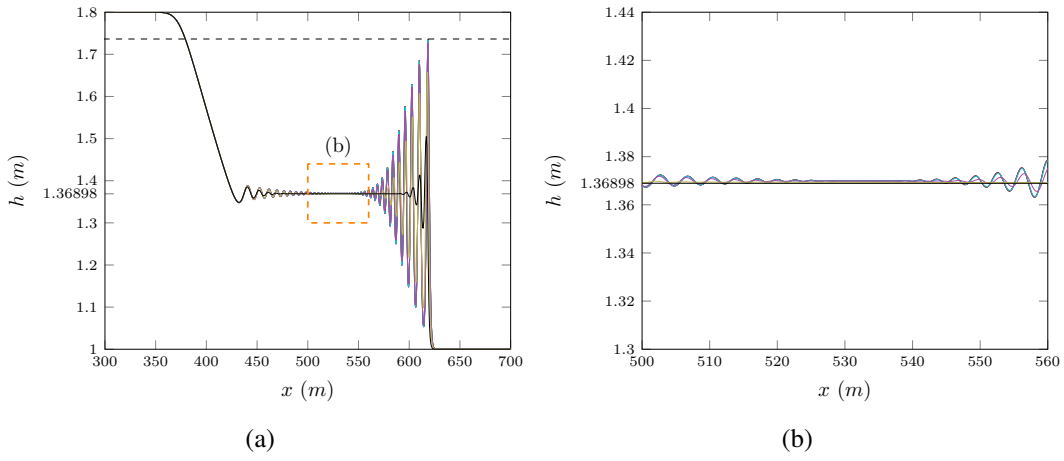


FIG. 8: Numerical results of  $\mathcal{V}_3$  at  $t = 30s$  for the smooth dam break problem with  $\beta = 5.8888$  for  $\Delta x = 10/2^{10}$  (blue solid),  $\Delta x = 10/2^9$  (green solid),  $\Delta x = 10/2^8$  (red solid),  $\Delta x = 10/2^7$  (cyan solid),  $\Delta x = 10/2^6$  (purple solid),  $\Delta x = 10/2^5$  (yellow solid),  $\Delta x = 10/2^4$  (black solid) with reference value  $a^+$  (black dashed).

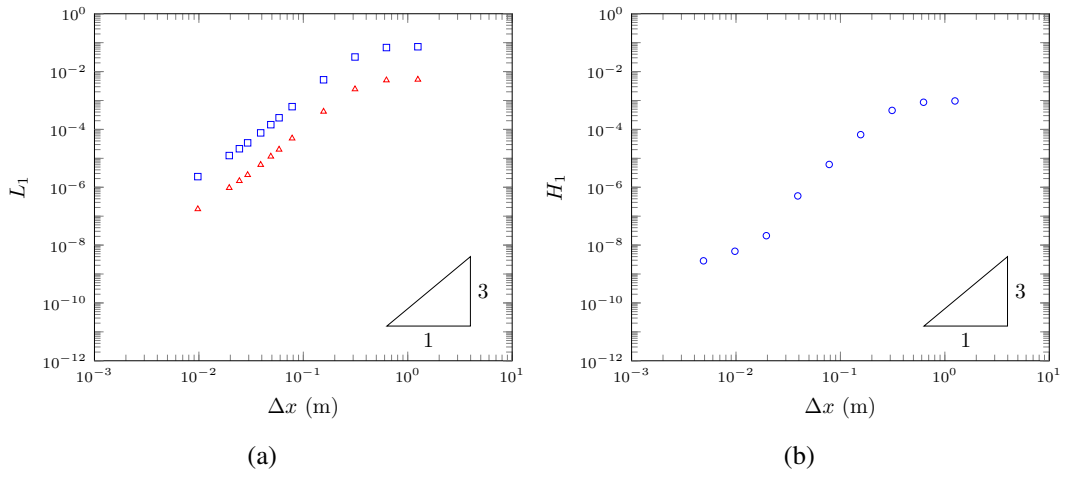


FIG. 9:  $L_1$  for  $h$  ( $\Delta$ ) and  $u$  ( $\square$ ) and  $H_1$  ( $\circ$ ) for  $V_3$ 's solution for the smooth dam-break problem with  $\beta = 5.8888$ .

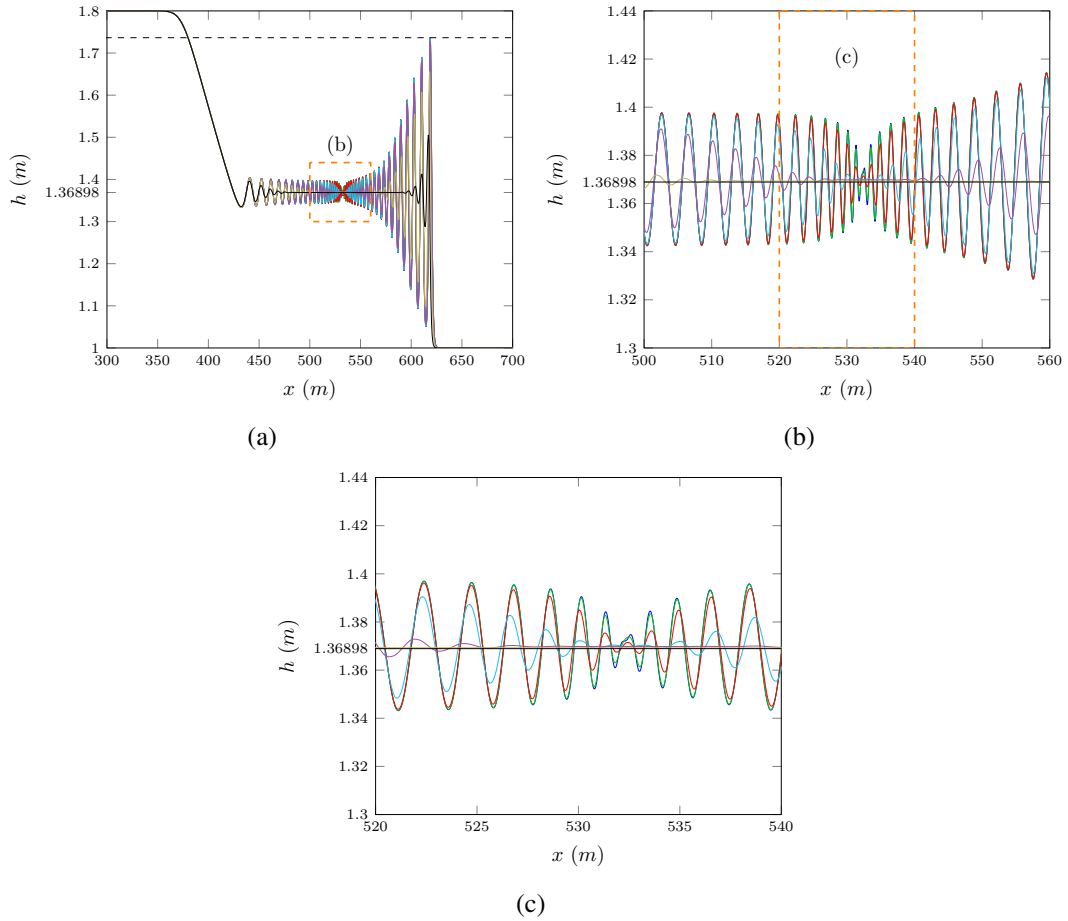


FIG. 10: Numerical results of  $\mathcal{V}_3$  at  $t = 30s$  for the smooth dam break problem with  $\beta = 1.17778$  for  $\Delta x = 10/2^{10}$  (blue),  $\Delta x = 10/2^9$  (green),  $\Delta x = 10/2^8$  (red),  $\Delta x = 10/2^7$  (cyan),  $\Delta x = 10/2^6$  (purple),  $\Delta x = 10/2^5$  (yellow),  $\Delta x = 10/2^4$  (black) with reference value  $a^+$  (dashed).

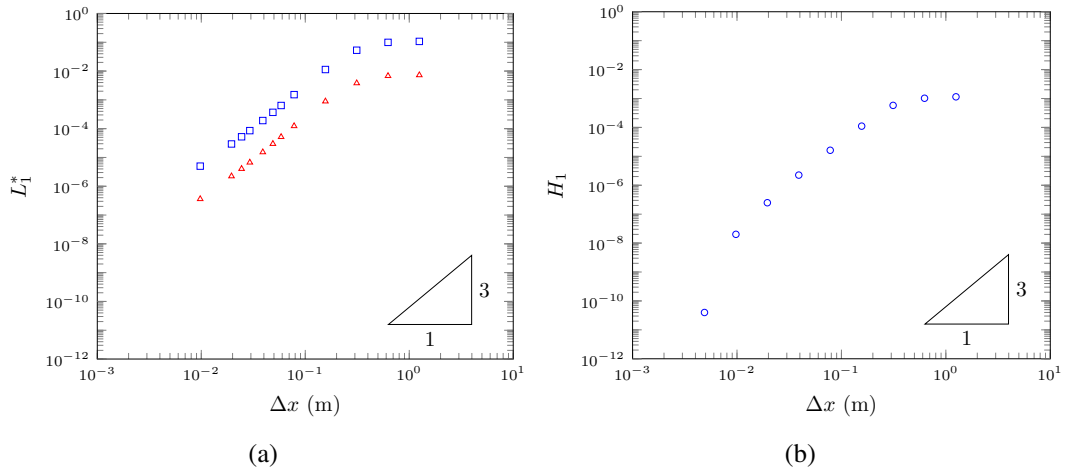


FIG. 11:  $L_1^*$  for  $h$  ( $\triangle$ ) and  $u$  ( $\square$ ) and  $H_1$  ( $\circ$ ) for  $\mathcal{V}_3$ 's solution for the smooth dambreak problem with  $\beta = 1.17778$ .

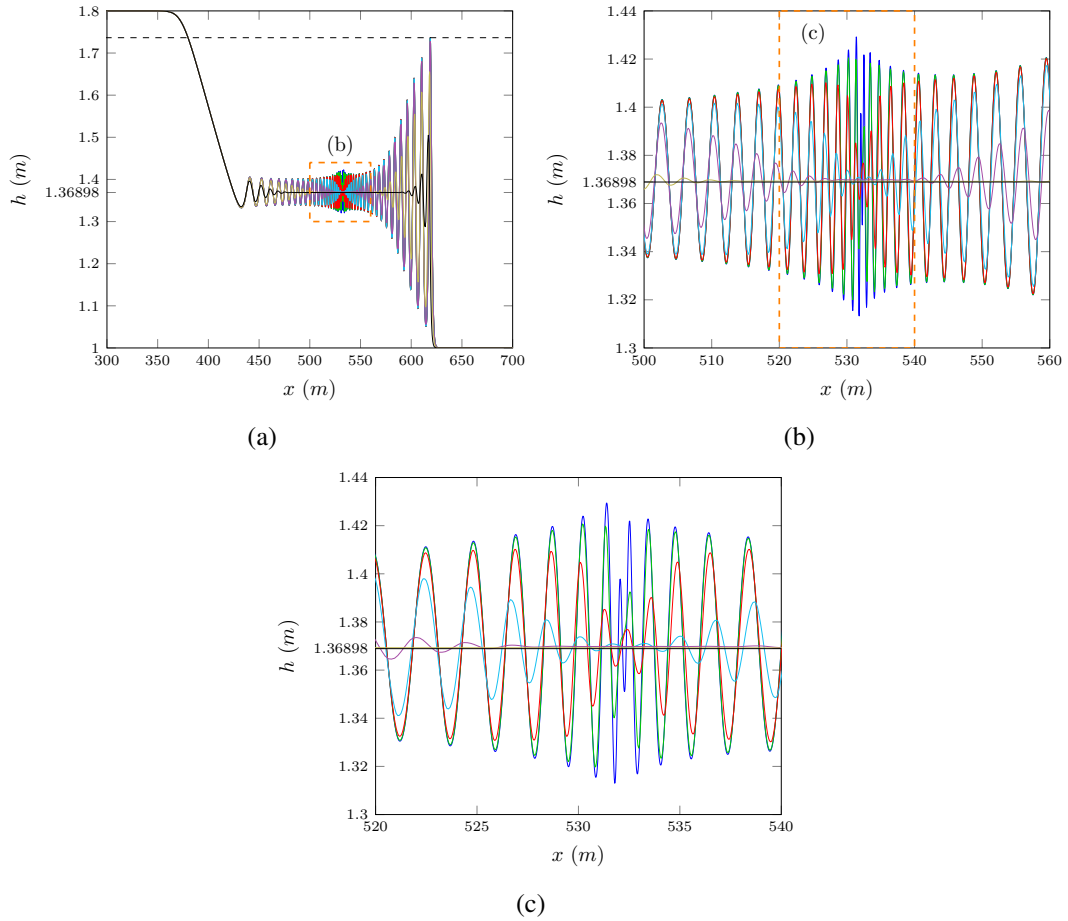


FIG. 12: Numerical results of  $\mathcal{V}_3$  at  $t = 30s$  for the smooth dam break problem with  $\beta = 0.294$  for  $\Delta x = 10/2^{10}$  (—),  $\Delta x = 10/2^9$  (—),  $\Delta x = 10/2^8$  (—),  $\Delta x = 10/2^7$  (—),  $\Delta x = 10/2^6$  (—),  $\Delta x = 10/2^5$  (—),  $\Delta x = 10/2^4$  (—) with reference value  $a^+$  (---).

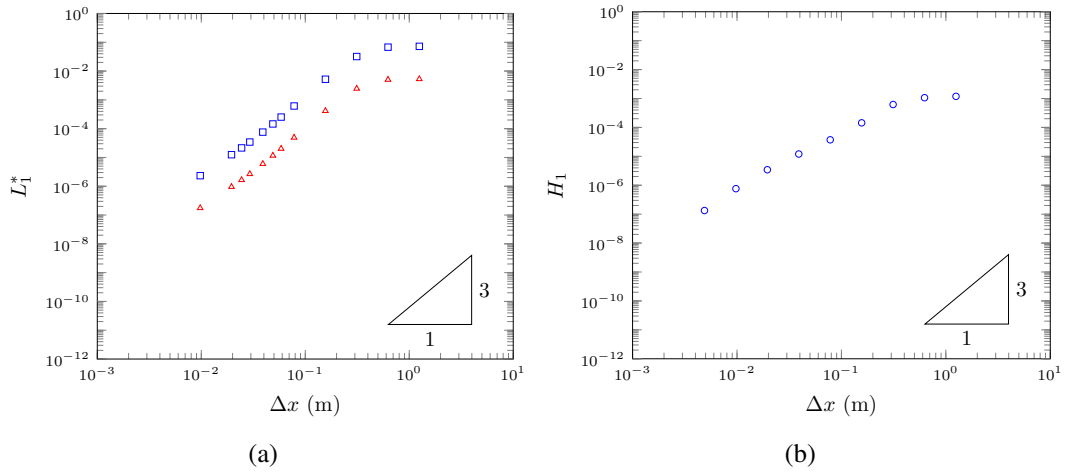


FIG. 13:  $L_1^*$  for  $h$  ( $\triangle$ ) and  $u$  ( $\square$ ) and  $H_1$  ( $\circ$ ) for  $\mathcal{V}_3$ 's solution for the smooth dambreak problem with  $\beta = 0.294$ .

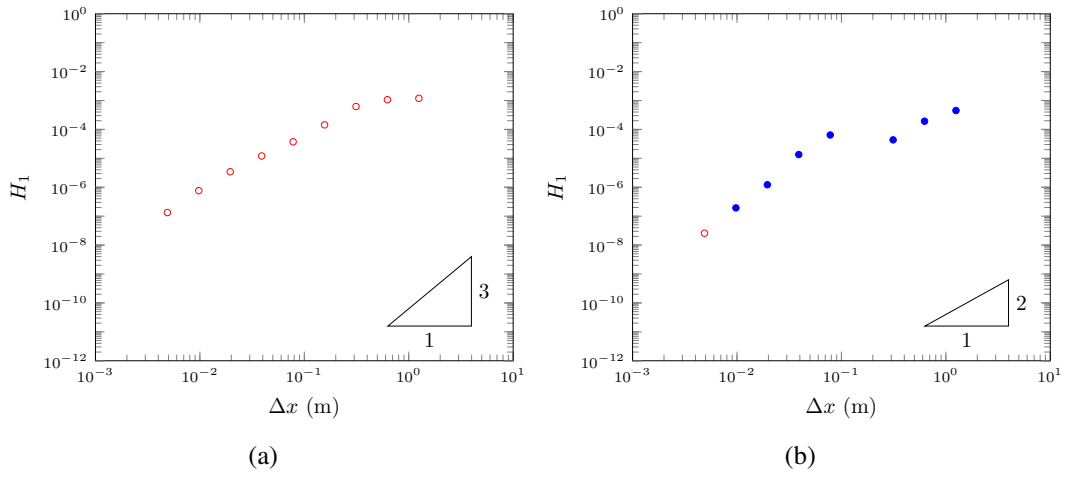


FIG. 14:  $H_1$  for  $\mathcal{V}_3$  (a) and  $\mathcal{G}$ 's (b) solution for the smooth dambreak problem at  $t = 30s$  with  $\beta = 0.294$  demonstrating when  $\mathcal{H}(0s) \geq \mathcal{H}(30s)$  (○) and  $\mathcal{H}(0s) < \mathcal{H}(30s)$  (●).

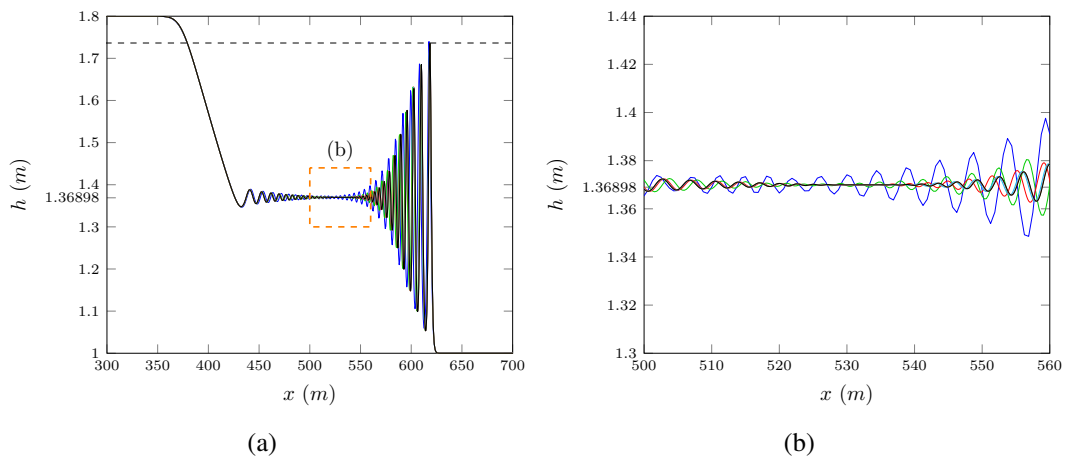


FIG. 15: Numerical results of  $\mathcal{G}$  at  $t = 30s$  for the smooth dam break problem with  $\beta = 5.8888$  for  $\Delta x = 10/2^4$  (blue solid),  $\Delta x = 10/2^5$  (green solid),  $\Delta x = 10/2^6$  (red solid),  $\Delta x = 10/2^7$  (cyan solid),  $\Delta x = 10/2^8$  (purple solid),  $\Delta x = 10/2^9$  (yellow solid),  $\Delta x = 10/2^{10}$  (black solid) with reference value  $a^+$  (dashed)

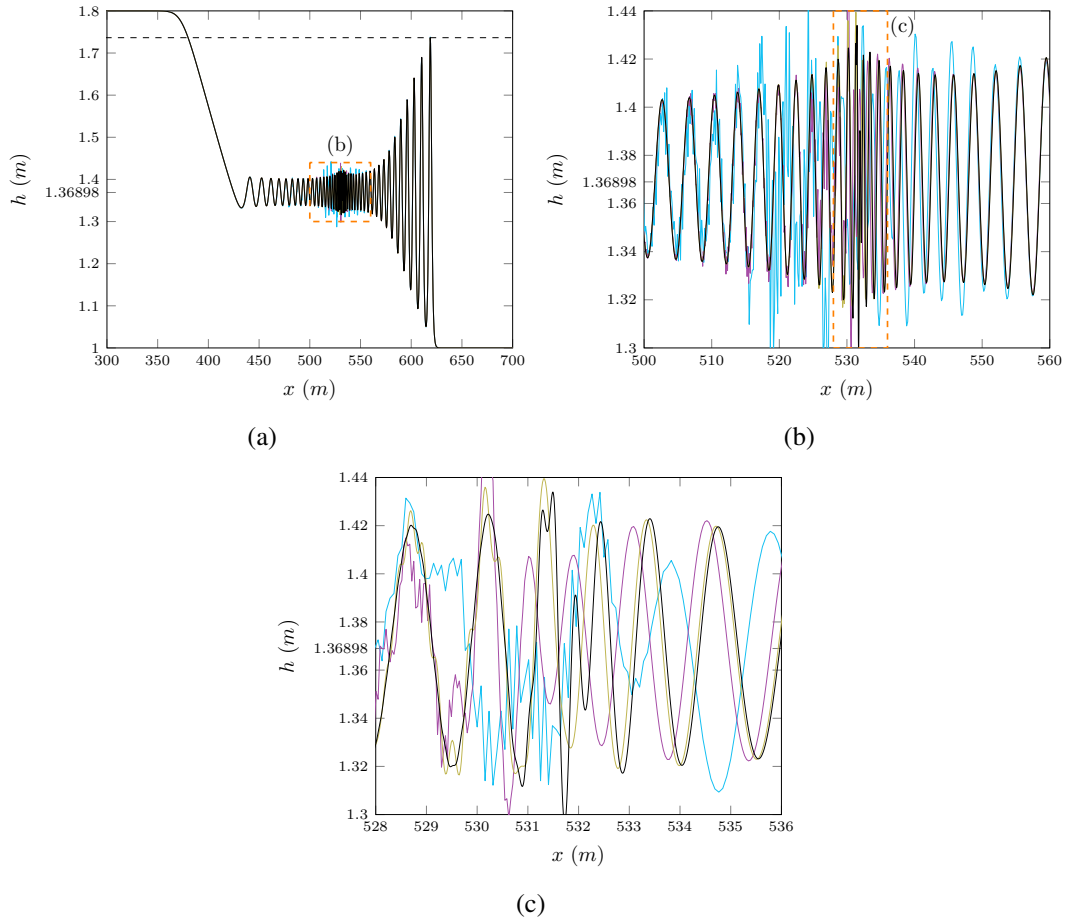


FIG. 16: Numerical results of  $\mathcal{G}$  at  $t = 30s$  for the smooth dam break problem with  $\beta = 0.294$  for  $\Delta x = 10/2^7$  (—),  $\Delta x = 10/2^8$  (—),  $\Delta x = 10/2^9$  (—),  $\Delta x = 10/2^{10}$  (—) with reference value  $a^+$  (— —)

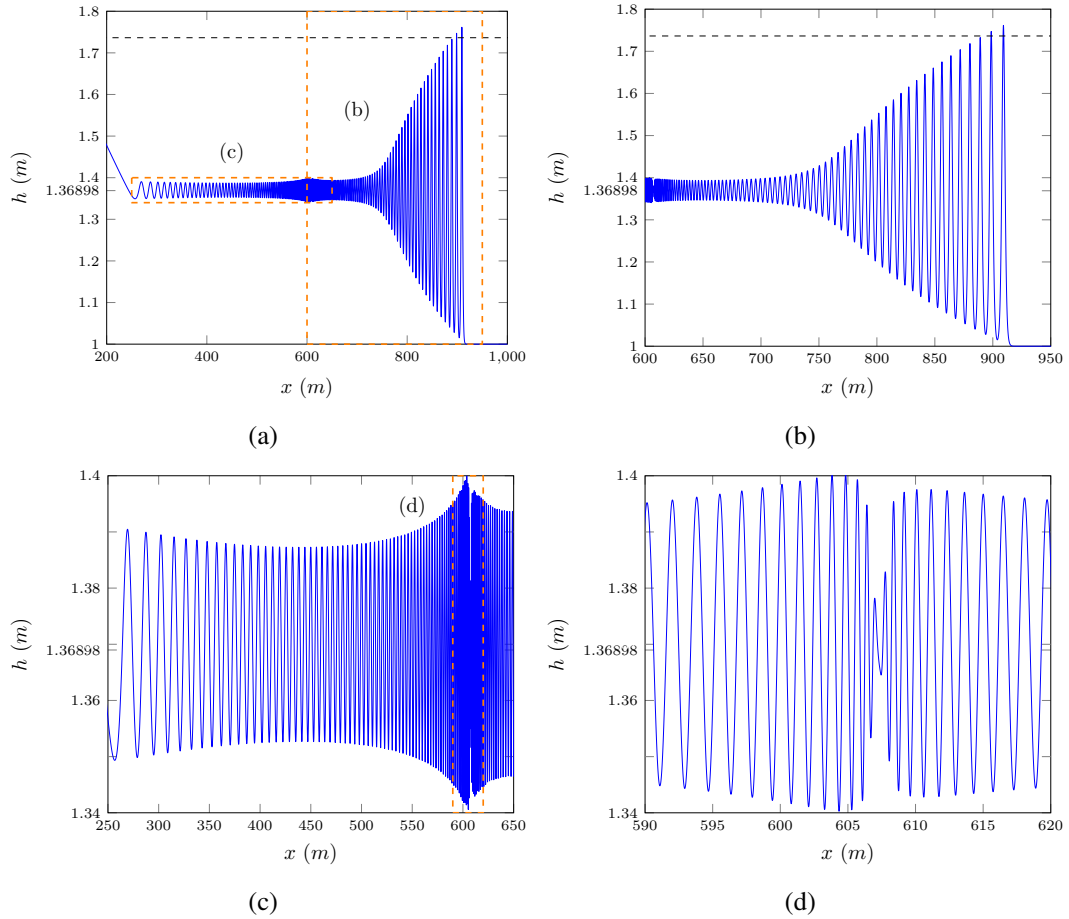
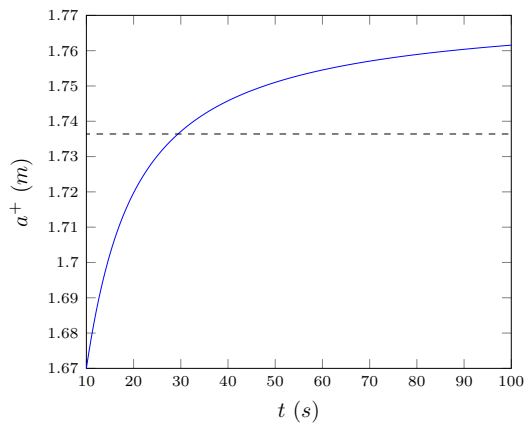


FIG. 17: Smooth dam break problem at  $t = 100s$  for  $\mathcal{V}_3$  with  $\beta = 0.294$  for  $\Delta x = 10/2^{10}$  (—) with reference value  $a^+$  (---).



(a)

FIG. 18: Lead soliton height plotted over time for the smooth dam break problem at  $t = 100s$  for  $\mathcal{V}_3$  with  $\beta = 0.294$  for  $\Delta x = 10/2^{10}$  (—) with reference value  $a^+$  (---).

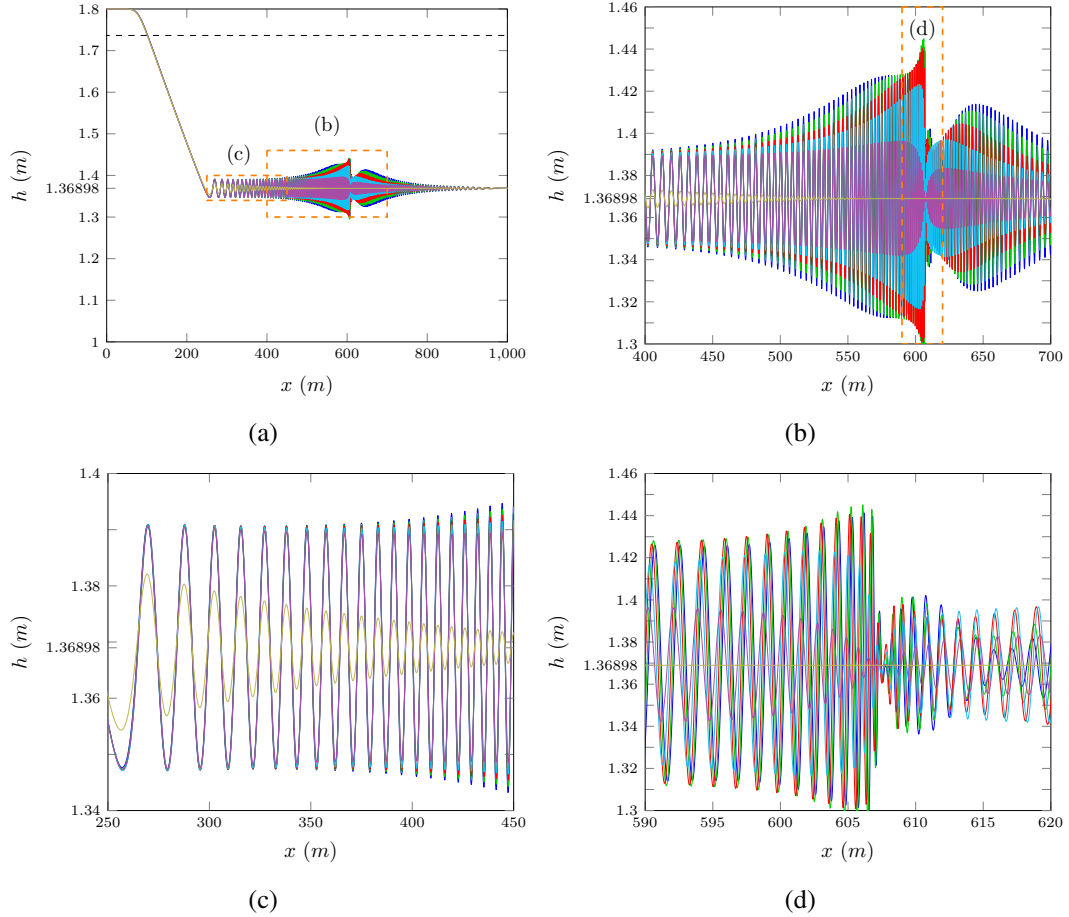


FIG. 19: Numerical results of  $\mathcal{V}_3$  at  $t = 100s$  for the smooth dam break rarefaction fan for  $\Delta x = 10/2^{10}$  with  $\beta = 0.2944$  (blue),  $\beta = 0.3464$  (green),  $\beta = 0.4530$  (red),  $\beta = 0.6543$  (cyan),  $\beta = 1.1778$  (purple), and  $\beta = 5.8888$  (yellow).

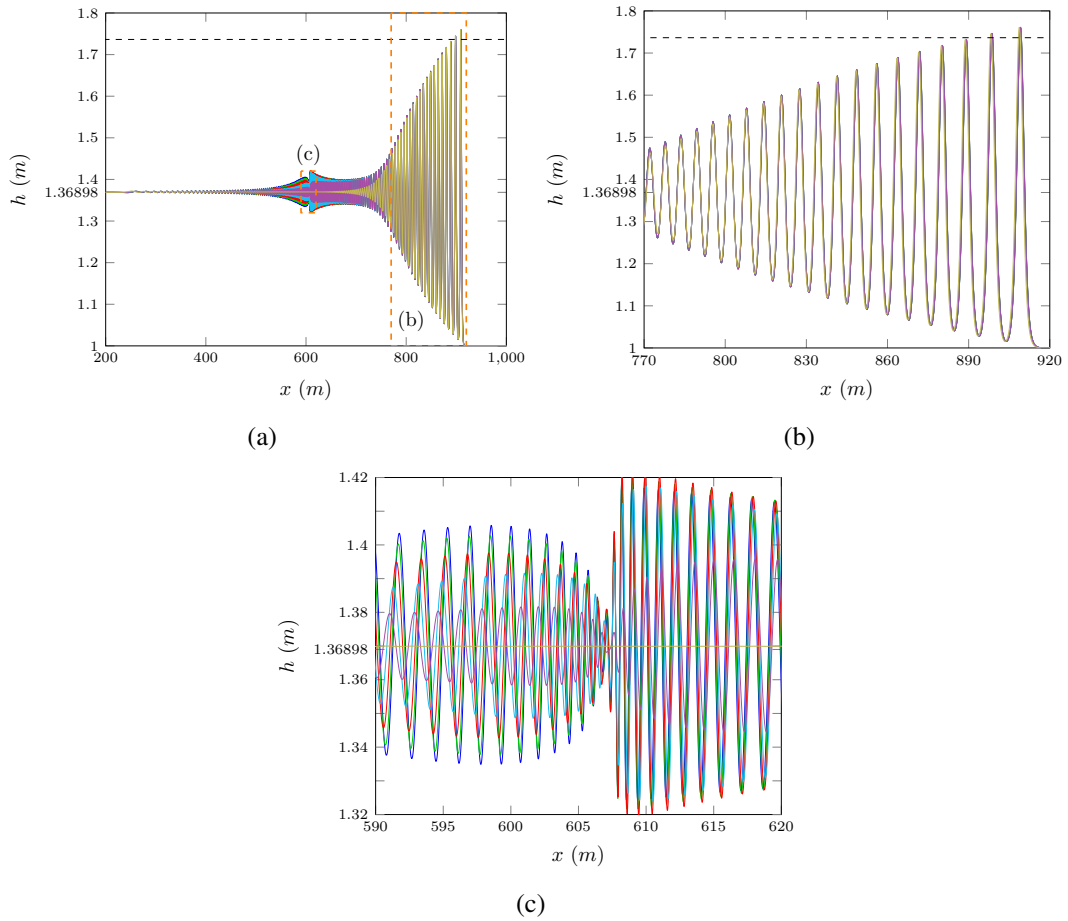


FIG. 20: Numerical results of  $\mathcal{V}_3$  at  $t = 100s$  for the smooth dam break shock wave for  $\Delta x = 10/2^{10}$  with  $\beta = 0.2944$  (blue),  $\beta = 0.3464$  (green),  $\beta = 0.4530$  (red),  $\beta = 0.6543$  (cyan),  $\beta = 1.1778$  (purple) and  $\beta = 5.8888$  (yellow).

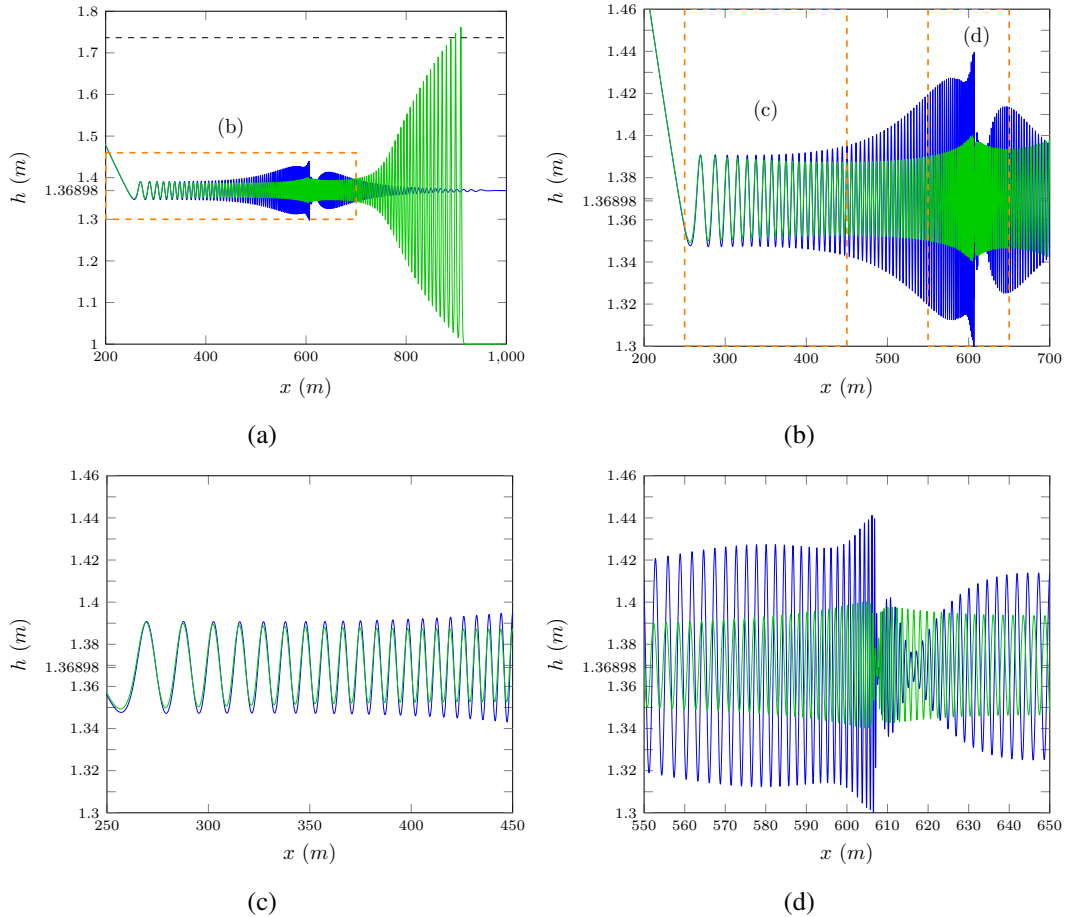


FIG. 21: Numerical results of  $\mathcal{V}_3$  at  $t = 100s$  for the smooth dam break  $\beta = 0.2944$  (—) and the smooth dam break shock wave (—),  $\beta = 0.2944$  for  $\Delta x = 10/2^{10}$ .

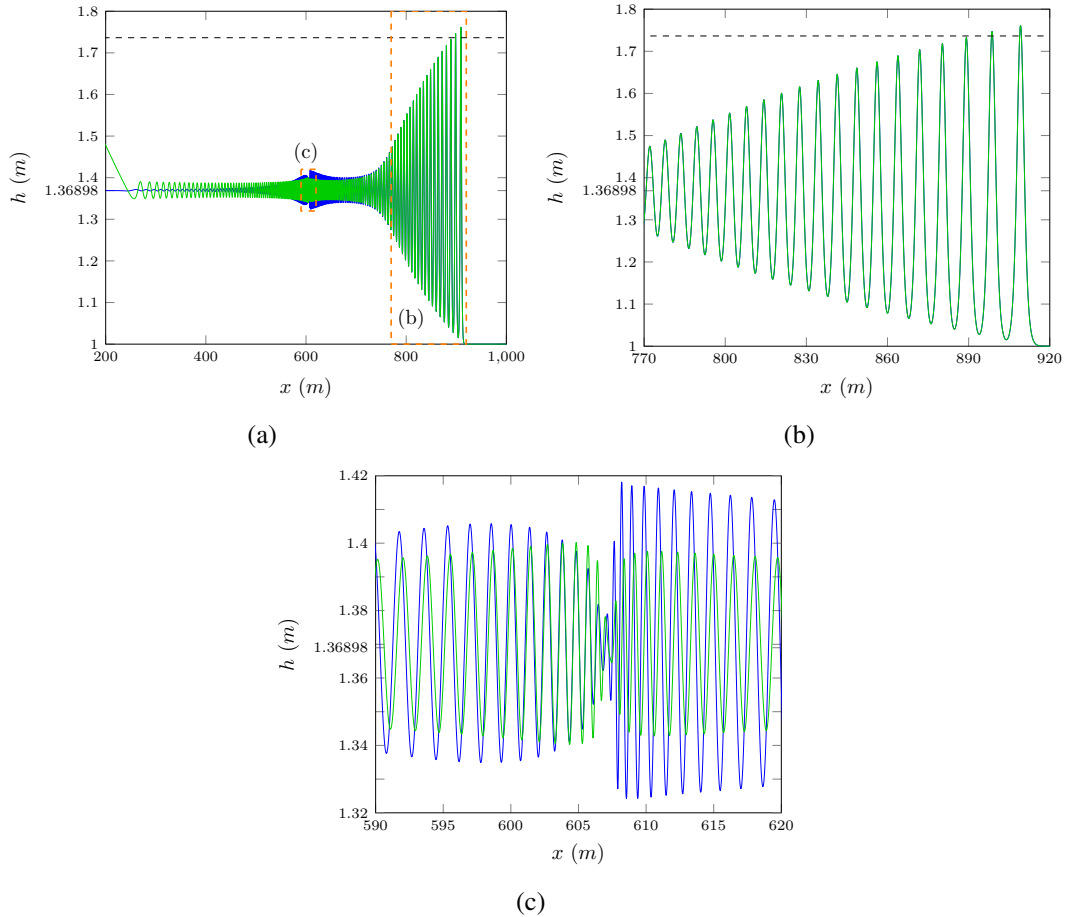


FIG. 22: Numerical results of  $\mathcal{V}_3$  at  $t = 100$ s for the smooth dam break  $\beta = 0.2944$  (—) and the smooth dam break shock wave  $\beta = 0.2944$  (—) for  $\Delta x = 10/2^{10}$ .

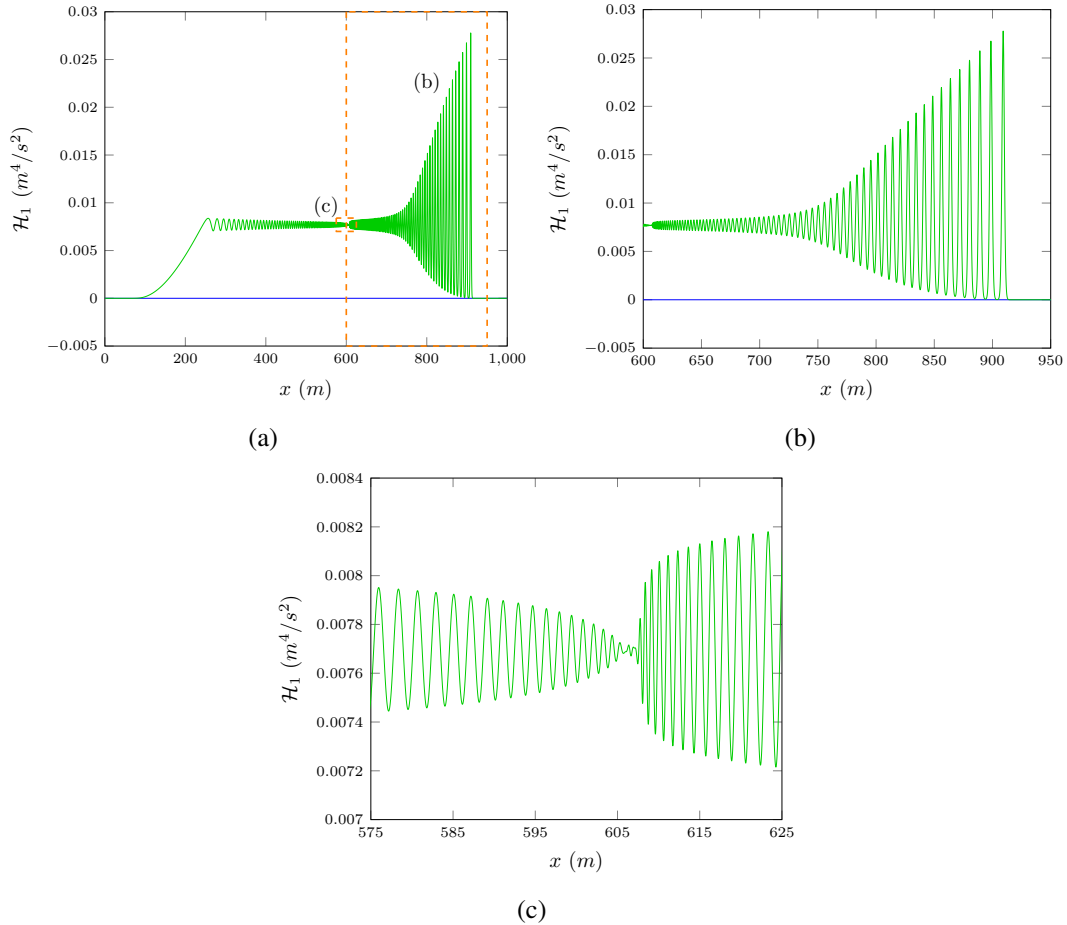


FIG. 23:  $\mathcal{H}_1$  for  $\mathcal{V}_3$  solution of the smooth dam break with  $\beta = 0.2944$  and  $\Delta x = 10/2^{10}$  at  $t = 0s$  (—) and  $t = 100s$  (—).

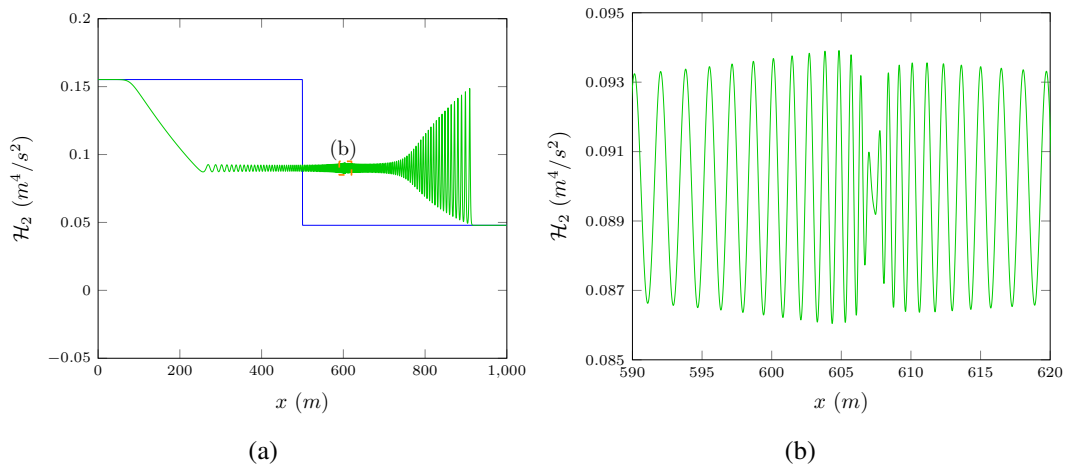


FIG. 24:  $\mathcal{H}_2$  for  $\mathcal{V}_3$  solution of the smooth dam break with  $\beta = 0.2944$  and  $\Delta x = 10/2^{10}$  at  $t = 0\text{s}$  (—) and  $t = 100\text{s}$  (—).

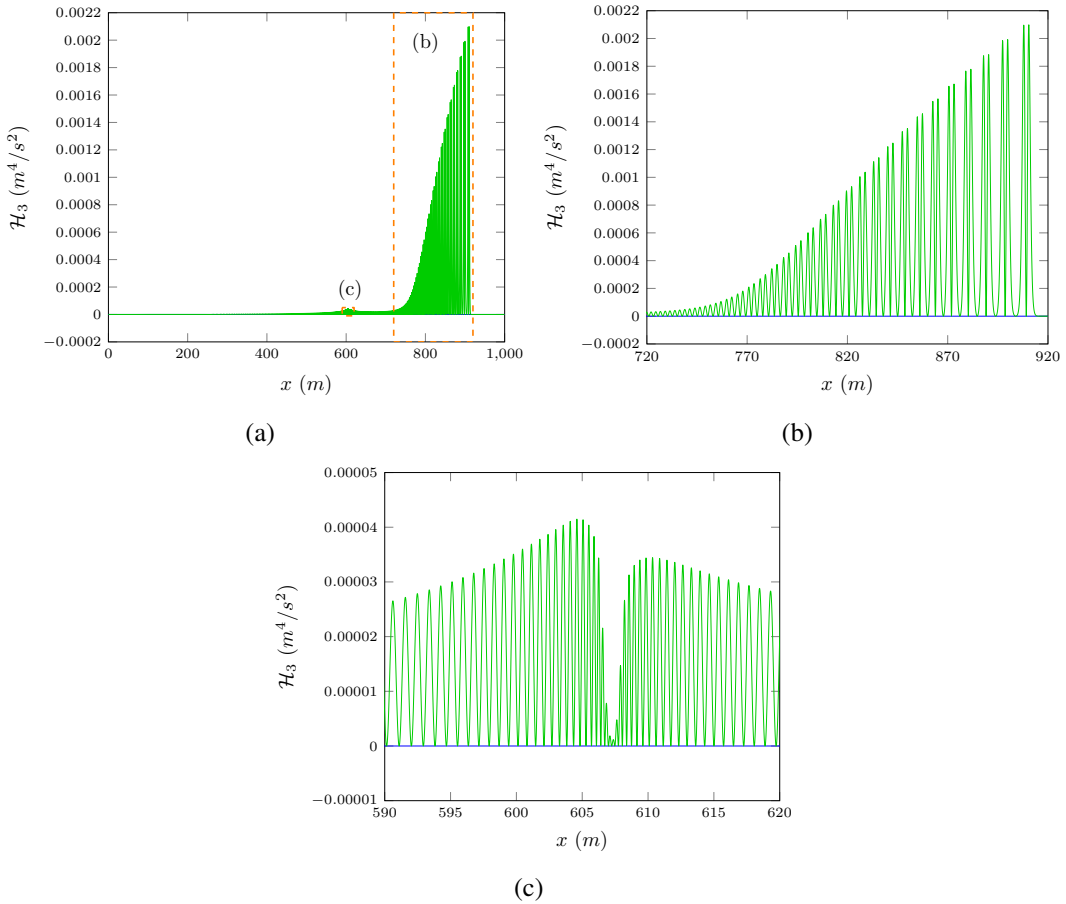


FIG. 25:  $\mathcal{H}_3$  for  $\mathcal{V}_3$  solution of the smooth dam break with  $\beta = 0.2944$  and  $\Delta x = 10/2^{10}$  at  $t = 0s$  (blue) and  $t = 100s$  (green).

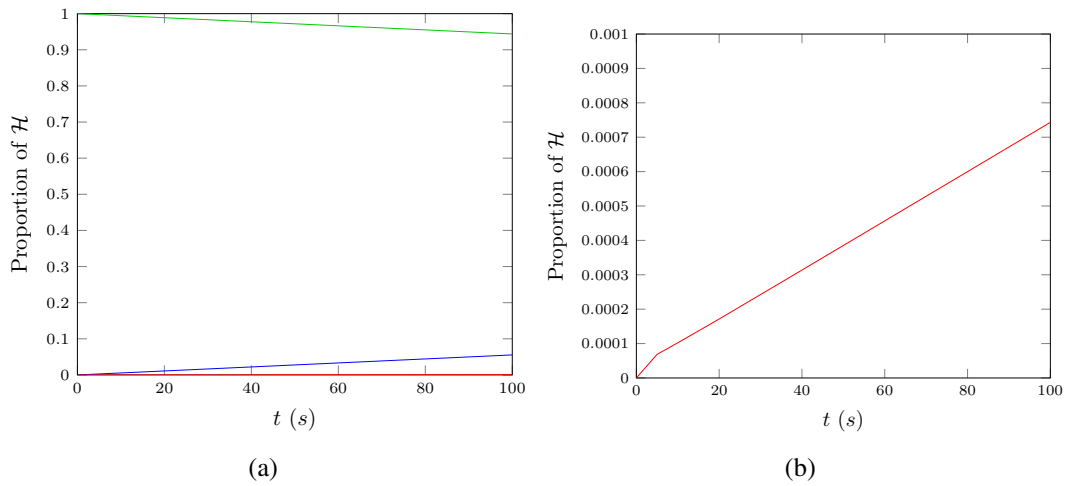


FIG. 26: Proportion of  $\mathcal{H}$  made up by  $\mathcal{H}_1$  (—),  $\mathcal{H}_2$  (—) and  $\mathcal{H}_3$  (—) for  $\mathcal{V}_3$  solution of the smooth dam break with  $\beta = 0.2944$  and  $\Delta x = 10/2^{10}$  over time.

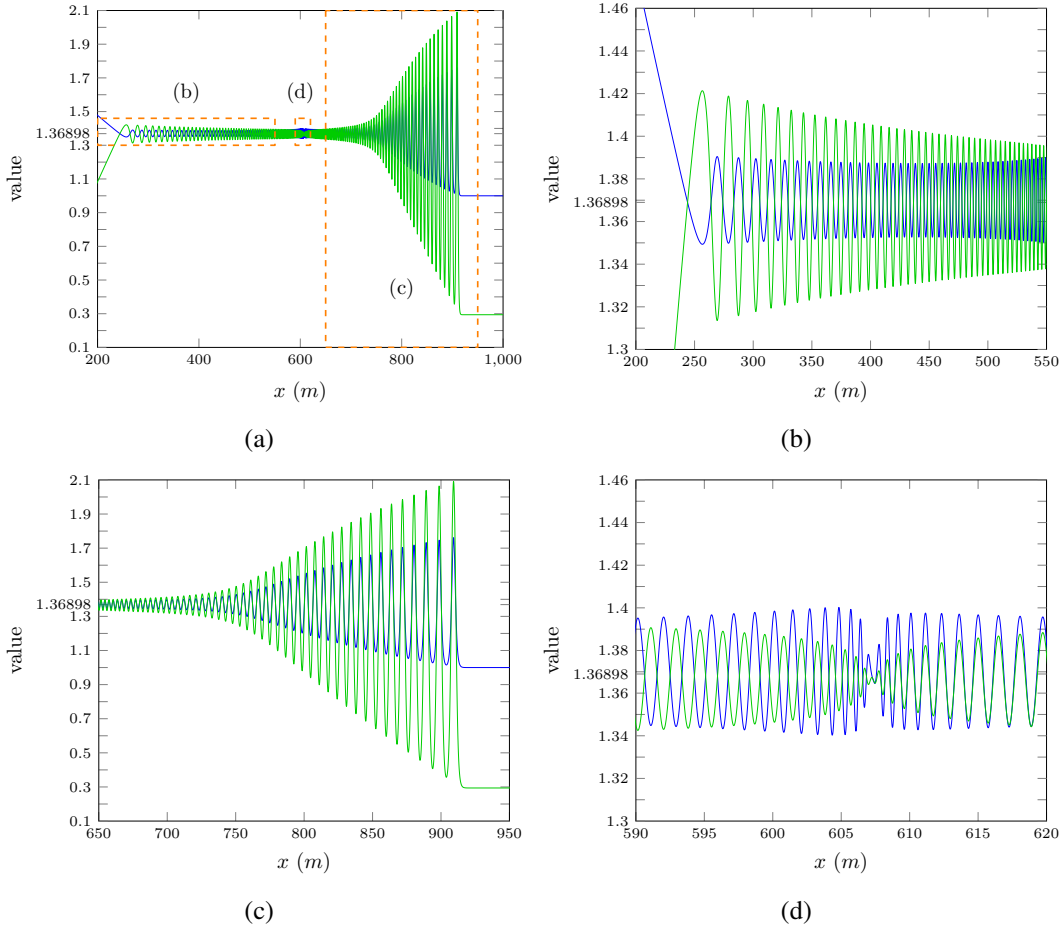
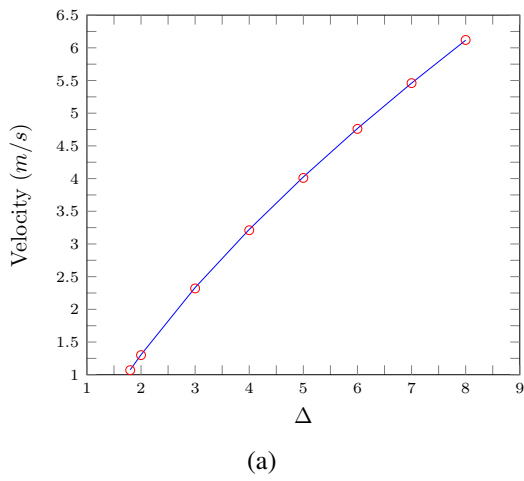


FIG. 27:  $h$  (—) and adjusted  $u$  (—) for  $\mathcal{V}_3$  solution of the smooth dam break with  $\beta = 0.2944$  and  $\Delta x = 10/2^{10}$  at  $t = 100s$ .



(a)

FIG. 28:  $v_{DB}$  (—) and  $v_{CD}$  (○) for  $\mathcal{V}_3$  solution of the various smooth dam break problems with  $\beta = 0.2944$  and  $\Delta x = 10/2^{10}$  at  $t = 100s$ .